Dissolving microarray patches for transdermal delivery of risperidone for schizophrenia management

Ghanma, R., Naser, Y., Anjani, Q. K., Sabri, A. H. B., Hutton, A. R. J., Vora, L. K., Himawan, A., Moreno-Castellanos, N., Greer, B., McCarthy, H. O., Paredes, A. J., & Donnelly, R. F. (2024). Dissolving microarray patches for transdermal delivery of risperidone for schizophrenia management. *International journal of pharmaceutics*, *660*, Article 124342. Advance online publication. https://doi.org/10.1016/j.ijpharm.2024.124342

Link to publication record in Ulster University Research Portal

Dissolving microarray patches for transdermal delivery of risperidone for schizophrenia management

Rand Ghanma [a,b], Yara A. Naser [a], Qonita Kurnia Anjani [a], Akmal Hidayat Bin Sabri [a], Aaron R.J. Hutton [a], Lalitkumar K. Vora [a], Achmad Himawan [a,c], Natalia Moreno-Castellanos [d], Brett Greer [e], Helen O. McCarthy [a], Alejandro J. Paredes [a], Ryan F. Donnelly [a,*]

[a] *School of Pharmacy, Queen's University Belfast, Medical Biology Centre, 97 Lisburn Road, Belfast BT9 7BL, UK*
[b] *Department of Pharmaceutical Technology, Faculty of Pharmacy, Jordan University of Science and Technology, Irbid, Jordan*
[c] *Department of Pharmaceutical Science and Technology, Faculty of Pharmacy, Universitas Hasanuddin, Makassar 90245, Indonesia*
[d] *Basic Science Department, Faculty of Health, Universidad Industrial de Santander, Bucaramanga 680001, Colombia*
[e] *Institute for Global Food Security, School of Biological Science, Queen's University Belfast, 19 Chlorine Gardens, Belfast BT9 5DL, UK*

ARTICLE INFO

ABSTRACT

Schizophrenia is a psychiatric disorder that results from abnormal levels of neurotransmitters in the brain. Risperidone (RIS) is a common drug prescribed for the treatment of schizophrenia. RIS is a hydrophobic drug that is typically administered orally or intramuscularly. Transdermal drug delivery (TDD) could potentially improve the delivery of RIS. This study focused on the development of RIS nanocrystals (NCs), for the first time, which were incorporated into dissolving microneedle array patches (DMAPs) to facilitate the drug delivery of RIS. RIS NCs were formulated *via* wet-media milling technique using poly(vinylalcohol) (PVA) as a stabiliser. NCs with particle size of 300 nm were produced and showed an enhanced release profile up to 80 % over 28 days. *Ex vivo* results showed that 1.16 ± 0.04 mg of RIS was delivered to both the receiver compartment and full-thickness skin from NCs loaded DMAPs compared to 0.75 ± 0.07 mg from bulk RIS DMAPs. In an *in vivo* study conducted using female Sprague Dawley rats, both RIS and its active metabolite 9-hydroxyrisperidone (9-OH-RIS) were detected in plasma samples for 5 days. In comparison with the oral group, DMAPs improved the overall pharmacokinetic profile in plasma with a $\sim$ 15 folds higher area under the curve (AUC) value. This work has represented the novel delivery of the antipsychotic drug, RIS, through microneedles. It also offers substantial evidence to support the broader application of MAPs for the transdermal delivery of poorly water-soluble drugs.

1. Introduction

Approximately 0.32 % of the global population, or about 24 million people, suffer with schizophrenia, a neurological condition marked by profound distortions in perceiving reality and accompanying behavioural changes (Schizophrenia, (n.d.). https://www.who.int/news-room/fact-sheets/detail/schizophrenia (accessed March 19, 2024). This disorder manifests through symptoms like delusions, hallucinations, disorganised speech or behaviour, and impaired cognitive function. The origin of these symptoms lies in an imbalance of neurotransmitters, including dopamine and serotonin (Patel et al., 2014). Risperidone (RIS), an antipsychotic medication, is used to treat schizophrenia and related disorders. It operates by antagonising serotonin-5HT2 and dopamine-D2 receptors, with its hydrophobic nature placing it within Biopharmaceutical Classification System (BCS) class II (Khames, 2017). RIS is available in various forms—tablets, oral solutions, and injections (D'Souza et al., 2013; Al-Akayleh et al., 2020). While oral doses require frequent administration and long-acting injections can be painful, necessitating healthcare professional involvement, transdermal drug delivery (TDD) presents an appealing alternative. TDD systems offer advantages such as non-invasiveness and ease of self-administration, thereby promoting patient adherence (Prausnitz and Langer, 2008). However, in conventional TDD, the *stratum corneum* (SC) layer, the outermost layer of the skin, presents a potential limitation to drug absorption for conventional TDD (Wiechers, 1989). This layer consists of dead cells called corneocytes along with an

extracellular lipid matrix, which collectively form the skin's barrier function (Wiechers, 1989).

As an alternative of conventional transdermal patches, microneedles (MNs), or microneedle array patches (MAPs), have emerged as a promising strategy for enhancing drug permeation across the skin. These micron-sized needles, typically ranging from 50 to 900 μm in height and with a density of up to 2000 MN/cm^2, are solidly anchored on a substrate. Upon insertion into the skin, they create microconduits by puncturing the SC (Ramadon et al., 2022; Menon et al., 2021). MAPs encompass diverse types—solid, hollow, coated, dissolving, and hydrogel-forming. Dissolving MAPs (DMAPs), constructed from biodegradable polymers carrying targeted drugs, commence dissolution upon contact with interstitial fluids post-insertion, thereby facilitating drug release (Guillot et al., 2020; Vora et al., 2021). Hydrophilic molecules are often paired with DMAPs due to the water-soluble nature of the polymer matrix. In contrast, the incorporation of hydrophobic compounds in DMAPs presents challenges due to their limited aqueous solubility (Vora et al., 2018). Overcoming this hurdle necessitates the generation of nano-sized particles, which not only enhances solubility, but also fosters uniform drug dispersion within the DMAPs matrix (Abdelghany et al., 2019).

Among the various nano-sized formulations, nanocrystals (NCs) possess intriguing qualities, particularly when integrated into DMAPs. NCs, composed solely of the therapeutic substance, can attain 100 % drug content and maintain stability with minimal stabiliser use. Moreover, their production employs relatively straightforward methods that are amenable to scaling up compared to other nano-sized drug delivery systems (Paredes et al., 2020). Prior work has produced RIS NCs utilising techniques like solvent-anti-solvent precipitation, combined nanoprecipitation and probe sonication, and a blend of nano-precipitation with high-pressure homogenization (Gol et al., 2018). These methods involve organic solvents for drug solubilisation. In our present work, we demonstrated, for the first time, the application of laboratory-scale wet-milling to generate RIS NCs, following the precedent set by the majority of market-reached NCs products (Kulkarni and Myerson, 2017). Subsequently, diverse DMAPs formulations were developed and characterised, incorporating NCs or bulk RIS. These fabricated DMAPs were then evaluated for their pharmacokinetic profiles in *in vivo* studies using female Sprague Dawley rats, with both RIS and its active metabolite 9-hydroxyrisperidone (9-OH-RIS) quantified over a duration of 14 days. Oral administration of RIS served as a control in these studies.

2. Materials and methods

2.1. Materials

Risperidone (99.8 %) was purchased from Cangzhou Enke Pharmatech Co., Ltd (Hebei Province, China). We got PVP K-90 (MW 1,300 kDa) and Plasdone™ K-29/32 (PVP MW 58 kDa) from Ashland (Kidderminster, UK). Elga PURELAB DV 25 purification system, (Veolia Water Systems, Dublin, Ireland) was used for ultrapure water supply. The remaining materials were obtained from Fisher Scientific (Loughborough, UK) or Sigma-Aldrich (Dorset, UK) and were of analytical grade. Full-thickness neonatal porcine skins were obtained from stillborn piglets within 24 h *post-mortem* and stored at − 20 °C until use.

2.2. Preparation of risperidone nanocrystals

Nanocrystals of RIS (RIS NCs) were prepared using a top-down approach through the wet media-milling technique, as previously reported (Anjani et al., 2022; Permana et al., 2020). Different stabilizer solutions (2 % w/w PVA 9–10 KDa, 2 % w/w PVA 9–10 KDa: 2 % w/w PVP 58 KDa, 2 % w/w PVP 58 KDa, 2 % w/w P188, and 2 % w/w P407) were utilised, and their effect on particle size was studied before and after lyophilisation. To create RIS NCs, initially 300 mg of RIS was weighed into a 7.5 mL glass vial, followed by the addition of 2 mL of

ceramic beads (Chemco beads, Guangfu, China) of 0.1 – 0.2 mm in diameter and four 12 x 6 mm magnetic stirrers. Then, 6 mL of the stabiliser was added. The vials containing the mixtures were then placed on top of an IKA RCT Basic Magnetic Stirrer (IKA, Staufen, Germany) at 1,250 rpm for 20 h. After milling, the nanosuspensions were separated from the ceramic milling beads through filtration using a 200-mesh nylon sieve into a glass vial. Subsequently, the samples were frozen at −80 °C for a minimum of 1 h before being transferred into a benchtop freeze dryer (SP Scientific Ltd., Warminster, PA).

2.3. Characterisation of risperidone nanocrystals

The particle size and dispersion of the NCs were characterized with a NanoBrook Omni® analyzer (Brookhaven, New York, USA), which using dynamic light scattering (Demartis et al., 2022; Altuntaş et al., 2022; Anjani et al., 2023). The samples were diluted with deionised water and placed in a poly(styrene) cuvette cell. After 180 s of equilibration at 25 °C, the particle size and distribution were examined for 180 s at a scattering angle of 90°. Each sample was measured three times, and the measurements were performed in triplicate. To determine the actual drug content in the lyophilized NCs, 1 mg of the lyophilised powder was weighed in a 1.5 mL Eppendorf tube. A mixture solution of methanol and acetonitrile (1 mL) was added to each tube to dissolve the drug and precipitate the polymer. The samples were mixed using a vortex and then sonicated for 24 h at 37 °C. After centrifugation at 14,000 rpm for 10 min, the samples were subjected to HPLC analysis. The surface morphology of bulk RIS and lyophilized NCs powders was visualised using SEM TM3030 microscope (Hitachi, Krefeld, Germany) with a Quanta FEG 250. The samples were attached to carbon adhesive discs and fixed to an aluminium stub before observation. ATR-FTIR spectroscopy (Accutrac FT/IR-4100™ Series, Perkin Elmer, USA) was utilised to determine any chemical interaction between RIS and PVA 9–10 KDa during the preparation of the NCs. TGA Q50 (TA Instruments, Elstree, Hertfordshire, UK) was used to thermally analyze RIS, PVA 9–10 KDa, PM, and NCs. PXRD (Rigaku Corporation, Kent, England) and DSC Q100 (TA Instruments, Elstree, Hertfordshire, UK) were performed to assess the crystallinity of RIS, PVA 9–10 KDa, PM, and NCs (Anjani et al., 2021).

2.4. In vitro release study of risperidone nanocrystals

In vitro release of RIS NCs was performed and compared with bulk RIS using a dialysis membrane method as previously detailed (Jain et al., 2011). Dispersion of lyophilised NCs was prepared and transferred into Spectra-Por®, MWCO 12–14 kDa dialysis membranes (Spectrum Medical Industries, CA, USA). Equivalent quantities of bulk RIS were weighted and placed in other membranes. The membranes were clamped to prevent leaking and placed in bottles containing 100 mL of the release media which consisted of 1 % SLS in PBS (pH 7.4) to maintain sink conditions based on the saturated solubility of RIS in 1 % SLS in PBS which was 2.42 mg/mL as found experimentally. The bottles were put in an orbital shaker at 100 rpm and 37 °C. At predefined timepoints of 0.5, 1, 1.5, 2, 2.5, 3, 4, 6, 8, 10, 22, 24, 28, 32, 48, 168, 240, 336, 504 and 672 h (over 28 days), 1 mL aliquots of each bottle were taken and replaced with fresh release media. Samples were appropriately diluted when necessary prior to their HPLC analysis to quantify the amount of RIS released.

2.5. Fabrication of dissolving MAP loaded with bulk risperidone

To compare the release behaviour of NCs with bulk suspension of RIS, MAPs loaded with bulk RIS were fabricated using a bilayer casting technique (Wu et al., 2022; Anjani et al., 2022). For the fabrication of the first layer of MAPs, a polymer stock of 40 % w/w PVA (9–10 KDa) in deionized water was prepared and kept at 80 °C for 24 h. A 40 % w/w PVP (58 KDa) solution in deionized water was prepared and sonicated

for 24 h to obtain a transparent solution. These polymers were then mixed in a 1:1 ratio in a Falcon® tube, referred to as PP2. Using the Speedmixer™ (Hauschild Engineering, Harnm, Germany), formulations containing 10 %, 25 %, and 40 % w/w of RIS, denoted as F1, F2, and F3, respectively, were prepared by mixing with the corresponding percentage of PP2 at 3500 rpm for 5 min. Aliquots of the formulation were spread over silicone flat moulds. To facilitate the filling of MAP projections, the moulds were placed in a pressure chamber for 3 min at 5 bar. Excess formulation was carefully removed using a spatula. Silicone rings were then attached to the moulds using a 30 % w/w PVA (9–10 KDa) blend. The moulds containing the first layer were kept at room temperature for 24 h to ensure complete drying before casting the second layer. To cast the baseplate, a blend of 30 % w/w PVP (58 KDa), 1.5 % w/w glycerol, and up to 100 % w/w deionised water was prepared in a 50 mL Falcon® tube. The blend was sonicated overnight and then centrifuged at 5000 rpm for 15 min to remove air bubbles and achieve a homogeneous mixture. For each MAP, 600 μL of baseplate gel was cast using a positive pressure pipette. The moulds were centrifuged at 5000 rpm for 15 min and then placed on a flat surface at room temperature for 24 h. After that, the MAPs were gently removed from the moulds, and their sidewalls were cut using scissors.

2.6. Fabrication of dissolving MAP loaded with risperidone-nanocrystals

The formulation of NCs that maintained stable particle size after lyophilisation was selected to be used as the first layer of the NCs-loaded MAPs. The bilayer casting technique was employed for casting the NCs-loaded MAPs, but the preparation of the first layer was slightly modified (Anjani et al., 2023; Bin Sabri et al., 2023). In this case, the first layer was prepared by mixing the lyophilised NCs with deionized water in a 1:1.5 w/v ratio, which was rationalised based on the consistency of the resulting mixture. The specific mass of the relevant NCs formulation was accurately weighed in a SpeedMixer™ cup, and the necessary volume of deionized water was added. The mixture was then mixed using the SpeedMixer™ at 3,500 rpm for 5 min. Following that, the first and second layers of the MAPs were cast as described in Section 2.5.

2.7. Evaluation of mechanical characteristics of dissolving MAPs

The mechanical properties of MAPs were characterised by measuring the percentage reduction in needle height during a compression test (A. Hidayat Bin Sabri, Q. Kurnia Anjani, R.F. Donnelly, , 2021; Anjani et al., 2023; Anjani et al., 2021; Reyna et al., 2023). This characterisation was performed using a TA-TX2 Texture Analyser (TA) (Stable MicroSystems Ltd., Godalming, Surrey, U.K.) in compression mode. The height of five needles from the four sides of three MAPs was manually measured using a Leica EZ4 D stereomicroscope. These measurements were recorded before and after the compression test. During the test, the MAPs were attached to a cylindrical probe (with a cross-sectional area of 1.5 cm^2) that descended from the upper arm of the Texture Analyser apparatus. The MAPs were secured with double-sided adhesive tape, with the needles facing downwards. The probe was then lowered vertically at a speed of 0.5 mm/s, compressing the MAPs for 30 sec with a force of 32 N, simulating the force applied by a human thumb against a flat aluminum surface. The percentage reduction in needle height was calculated using **Equation (1)**.

$$Height\ reduction\ \% = \frac{H0 - H1}{H0}\ x\ 100\% \tag{1}$$

where H_0 is the height of the needles before the application of the compression force, and H_1 is the needle height after applying 32 N force for 30 sec.

2.8. Evaluation of insertion properties of dissolving MAPs

The insertion characteristics of MAPs were evaluated using eight layers of Parafilm® M as an artificial skin model, each with a thickness of 126 μm. This evaluation method was based on previous studies (Larraneta et al., 2014; Anjani et al., 2024). The MAP was positioned over the layers of Parafilm® M with its projections facing downwards. A force was applied by the thumb for a duration of 30 s. Afterward, each layer was carefully removed and inspected under a digital light microscope to count the number of holes created in each layer. The insertion percentage was calculated using **Equation (2)**.

$$Insertion\ \% = \frac{number\ of\ holes\ observed}{number\ of\ arrays\ in\ a\ MAP\ (600\ array)}\ x\ 100\% \tag{2}$$

The insertion into full-thickness excised neonatal porcine skin was also examined using an optical coherence tomography (OCT) microscope (EX1301 VivoSight®, Michelson Diagnostics Ltd., Kent, UK).

2.9. Ex vivo permeation and skin deposition studies

Ex vivo permeation studies were conducted on RIS MAPs using neonatal porcine skin with a full thickness of approximately 500 μm. The skin samples were obtained from stillborn piglets within 24 h of birth, carefully shaved, and stored frozen at −20 °C until needed. Before the experiment, the skin was thawed using PBS (pH 7.4) and attached to the donor compartment of the modified Franz diffusion cells apparatus, with the epidermis side facing upwards. Thumb pressure for 30 s was applied to insert the MAPs into the skin. To keep the MAPs from moving, a stainless steel weight was placed on top of each MAP. The donor compartments were filled with preheated 1 % SLS in PBS (pH 7.4) and placed over the receiver compartments. The two compartments were clamped together to ensure a secure attachment. To prevent evaporation of the dissolution media, the donor compartment and sampling arm orifice were covered with Parafilm® M. At predetermined time intervals (0.5, 1, 2, 3, 4, 6, 8, and 24 h), 200 μL samples were collected from the receiver compartment, and replaced with fresh 1 % w/v SLS in PBS (pH 7.4) media. After 24 h, the Franz diffusion cells apparatus was disassembled, and the skin was extracted to recover the deposited drug. The skin was cut into small pieces to ensure maximum extraction of RIS. These skin pieces were placed in 2 mL Eppendorf tubes, and 0.5 mL deionised water along with 2 metal beads were added to each tube. The samples were homogenized using a Tissue Lyser LT (Qiagen, Manchester, UK) at 50 Hz for 15 min. Next, 1 mL of methanol was added to each tube, and the samples were homogenized again at 50 Hz for another 15 min. Each mixture was transferred to a Falcon® tube containing 3.5 mL methanol, which was then sonicated for 30 min. The samples were thoroughly vortexed and then diluted at a 1:10 ratio using 1 % w/v SLS in PBS (pH 7.4). Finally, the diluted samples were centrifuged at 14,800 rpm for 10 min prior to HPLC analysis. This method for extracting RIS from the skin was developed and validated prior to the *ex vivo* skin deposition studies to determine the extraction efficiency of the method. This was done by cutting some pieces of full-thickness excised porcine skin (approximately 1 cm^2) and weighing them separately. After that, an aqueous blend of RIS was injected using a syringe between the epidermis and dermis layers of the skin. Each skin piece was weighed again to record the amount of drug injected. To keep the skin samples from drying out, they were put in weighing boats on top of tissue papers soaked in PBS (pH 7.4). After that, they were wrapped in aluminum foil and placed in the oven at 37 °C for 24 hr. They were then treated as detailed for the skin taken from Franz cells after 24 hr and the percentage recovery was calculated.

2.10. Biocompatibility studies

The cytotoxicity assessment of the NCs-loaded MAPs and the blank

MAPs formulations was conducted *in vitro* using 3-(4,5-dimethylthiazol-2-yl)2,5-diphenyltetrazolium bromide (MTT, Sigma Aldrich, St. Louis, MO, USA), live/dead, and picogreen assays on adult human dermal fibroblasts (HDFa) cells. HDFa cells (5×10^3 cells/well) were cultured in a 48-well plate using DMEM (Sigma-Aldrich, Saint Louis, USA) supplemented with 10 wt% fetal bovine serum (FBS) (Sigma-Aldrich, Saint Louis, USA) and 1 wt% penicillin–streptomycin aqueous solution (Sigma-Aldrich, Saint Louis, USA). For the MTT assay, cell viability was evaluated as follows: formulations with cells were exposed to MTT reagent at a concentration of 5 mg/mL after 48 h of culture and incubated for 5 h at 37 °C in a 5 % CO_2 atmosphere. After rinsing the formulations with PBS pH 7.4, DMSO was introduced to dissolve the formed formazan crystals. Absorbance at 570 nm was gauged using a Multiskan GO spectrophotometer (Thermo Fisher Scientific, USA). The live/dead assay scrutinised the impact of formulations on live and dead cell numbers and morphology. Cells cultured with or without formulations for 48 h were treated with Calcein AM and ethidium homodimer-1 (Thermo Fisher Scientific, Wilmington, DE, USA) and then incubated for 45 min at room temperature. Fluorescence microscopy was conducted using an Olympus BX53 fluorescence microscope (Olympus America Inc. Farmingdale, NY, USA), with ImageJ software (NIH, USA) used for image processing. To quantify the DNA content and thereby cell proliferation, the picogreen (DNA quantification) assay was employed, following these steps: The DNA standard was used to generate a calibration curve for determining unknown DNA concentrations. Cells with or without formulations were exposed to a leaching solution for 48 h, and then subjected to freeze-–thaw cycles at −80 °C in DNA-free water to induce cell death. Subsequently, a mixture of 100 µl of TE buffer, 71.3 µL of picogreen solution, and 28.7 µL of freeze-thawed cell samples was added to each well of a black 48-well plate. A control was prepared using media without cells. The mixture was gently agitated for 2 min on a shaker and then left to incubate at room temperature for 5 to 8 min in darkness. Fluorescence measurements were conducted with a Varioskan Flash Thermo Scientific plate reader (Thermo Fisher Scientific Inc, Waltham, MA, USA) at an excitation wavelength of 480 nm and an emission wavelength of 520 nm.

2.11. Instrumentation and chromatographic condition for analytical and bioanalytical methods

The concentrations of RIS for *in vitro* studies were measured *via* HPLC (Agilent Technologies 1220 Infinity UK Ltd, Stockport, UK). HPLC analysis was done using column (250 mm × 4.6 mm i.d. with 5 µm particle size). A sample analysis flow rate of 1 mL/min was selected, conducted at a temperature of 25 °C. The mobile phase utilized comprised 75 % methanol and 25 % acetonitrile as the organic phase, while the aqueous phase consisted of HPLC-grade water with 1 % v/v triethylamine (TEA). The pH was adjusted to 7.2 using phosphoric acid 85 %. The sample detection was conducted at a wavelength, λ, of 280 nm, with a sample injection volume of 20 µL. The HPLC assay employed in this study has been validated in accordance with the International Council on Harmonisation (ICH) 2005 guidelines (Text, 2023).

For *in vivo* studies, RIS and 9-OH-RIS plasma levels were measured using a developed and validated bioanalytical method using an Acquity UPLC i-Class system connected to a Xevo TQ-MS (triple quadrupole MS/MS) mass spectrometer (Waters, Manchester, UK). A Waters Symmetry® C18 column: 150 mm x 4.6 mm internal diameter, 5 µm packing was used in order to retain RIS and 9-OH-RIS at 35 °C. The mobile phase composed of 80 % ACN and 20 % of 10 mM ammonium formate with a flow rate of 0.5 mL/min. The injection volume of the sample was 5 µL. The validation of the bioanalytical method used in this work was validated according to the International Council on Harmonisation (ICH) 2019 guideline (European Medicines Agency, ICH guideline M10 on bioanalytical method validation, 2019). An analytical method with high sensitivity for both was needed as RIS is a potent drug with a therapeutic range of 1–10 ng/mL for risperidone and 10–70 ng/mL for 9-OH-RIS

(Zhang et al., 2005).

2.12. In vivo studies

Ethical approval for all *in vivo* experiments was obtained from the Biological Services Unit (BSU) at Queen's University Belfast. Experimentation was conducted under Procedure Project Licence number 2903. Additionally, all researchers involved in the project held personal licenses issued by the UK Home Office. The *in vivo* experiments were conducted in compliance with the guidelines of the European Laboratory Animal Science Associations and the European Convention for the protection of vertebrate animals used for experimental and other scientific purposes. The implementation of the 3Rs principles (replacement, reduction, and refinement) was adhered to during the experimental procedures. Prior to the experiment, 12 female Sprague Dawley rats (Charles River Laboratories, Harlow, UK), 8–10 weeks old, with a mean weight of 290.17 ± 28.90 g, were acclimated for a week to the conditions of the animal house. Female rather than male rats were selected for the study as they exhibit more consistent behavioral responses, they are less aggressive, which can reduce variability in experiments and make handling and housing easier, and typically have a smaller body size that can be beneficial in pharmacokinetic studies (Quirós Cognuck et al., 2020; Atrooz et al., 2021; Simpson and Kelly, 2012). Animals were separated into two cohorts, each comprising 6 rats. The control cohort received 1 mL of RIS oral suspension corresponding a dose of 17 mg/kg of RIS. The oral suspension was prepared by mixing RIS with a freshly prepared 5 % w/v solution of methyl cellulose to produce a final suspension with a final concentration of 5 mg/mL.

The second cohort (n = 6) received four NCs loaded MAPs. The dose given to each rat was approximately 17 mg/kg. Prior to the experiment, the dorsal hair of the rats was shaved using electric hair clippers (Remington Co., London, U.K.). After that, a depilatory hair removal cream (Boots Smooth Care hair removal cream sensitive, Boots, Nottingham, UK) was used to remove any remaining hair. The next day, the same anaesthetic gas was used to sedate the rats before the application of the MAPs onto a pinched section of skin on the back of the rats using firm thumb pressure. The MAPs were then covered with Microfoam™ adhesive tape, and kinesiology tape was afterwards wrapped around the backs of the rats to keep MAPs securely in place for 24 h.

Blood samples were taken at 1, 2, 4 and 6 h (n = 3) rats per cohort and then at 1, 2, 3, 5, 7, 10 and 14 days (n = 6) via tail vein bleeds and placed in 1.5 mL preheparinized microtubes. Blood samples were promptly centrifuged at 10,000 rpm for 3 min to facilitate the separation of the plasma from other blood components. The resultant supernatants were then put into the appropriate labelled microtubes and kept in a freezer at −20 °C for further analysis. At the end of the *in vivo* studies, rats were culled using carbon dioxide (CO_2) asphyxiation.

2.13. RIS extraction from plasma samples

To extract RIS and 9-OH-RIS from plasma samples 500 µL of Ethyl acetate was added into aliquots of 50 µL of rat plasma in 1.5 mL microtubes. The mixture was vortexed for 30 mins at 1,500 rpm to facilitate the extraction of RIS from plasma. Afterwards, samples were centrifuged at 153,000 rpm for 10 min at 25 °C. Subsequently, supernatants were collected and transferred into glass culture tubes that were placed in Zymark TurboVap®LV Evaporator Workstation at 2.5 psi and 40 °C for 15 min for the complete evaporation of the solvent. 50 µL of ACN was used to reconstitute the precipitated samples. After that, samples were vortexed for 30 sec and transferred into glass inserts with polymeric feet inside Agilent® vials prior to their bioanalysis using the LC MS/MS system.

2.14. Pharmacokinetic studies

Noncompartmental model for pharmacokinetic analysis (PK

analysis) was applied using PK Solver as an add-in tool to Microsoft® Excel 2013. After plotting the drug plasma concentration (ng/mL) versus the time (h), the maximum plasma concentration (C_{max}), the time of the maximum concentration (T_{max}), the mean half-life ($t_{1/2}$), the area under the drug concentration–time curve from time zero (t = 0) to the last experimental time point (t = 336 h) (AUC_{0-t}), the area under the drug concentration–time curve from time zero (t = 0) to infinity (AUC_{0-inf}), and the mean residence time (MRT), where obtained.

2.15. Statistical analysis

Statistical analysis was performed using GraphPad Prism® version 9.0 (GraphPad Software, San Diego, California, USA). The normality of the data was evaluated using the Shapiro-Wilk test. If the p-value obtained from the test was greater than 0.05, the data were considered to be normally distributed. For normally distributed data (parametric data), unpaired t-tests were used to compare two groups, while one-way analysis of variance (ANOVA) with Tukey's post hoc test was used to compare three or more groups.

3. Results and discussion

3.1. Preparation of risperidone nanocrystals

NCs were selected as the desired cargo for the MAPs due to their main advantage of being prepared from the pure drug with a minimal amount of stabiliser, allowing for a drug content of up to 100 % (Muller et al., 2011). Wet media milling technique, which can be applied in both laboratory and industrial settings without the need for organic solvents, was used to produce NCs (Romero et al., 2016). NCs with a particle size of approximately 300 nm were successfully produced using PVA, PVA: PVP solution, and P407 as polymeric stabilisers. These stabilizers played a crucial role in reducing the particle size by creating a steric adsorption barrier on the particle surface, preventing crystal growth or particle coalescence (Vora et al., 2018). However, neither the use of PVP nor P188 stabiliser solutions were able to produce nanoparticles. Therefore, the choice of stabiliser was significantly influenced by the drug molecule, possibly due to the interaction forces between the drug surface and stabiliser molecule, as well as the concentration of the stabiliser affecting the steric stabiliser layer around the particles, thus preventing the formation of van der Waals forces between particles (Tuomela et al., 2016).

The objective was to produce small particles to facilitate their loading into the dissolving MAPs, aiming to increase the drug loading and achieve homogeneous needles with improved mechanical properties. The effect of different commonly used stabilisers on particle size and polydispersity index (PDI) was investigated. Fig. 1A summarises the results of the NCs' particle sizes before and after lyophilisation. No significant changes ($p > 0.05$) were observed in the particle size of the NCs stabilised using PVA, indicating that no cryoprotectant is required. However, the particle sizes of NCs produced with PVA:PVP solution or P407 as stabilizers were significantly larger ($p < 0.05$) after

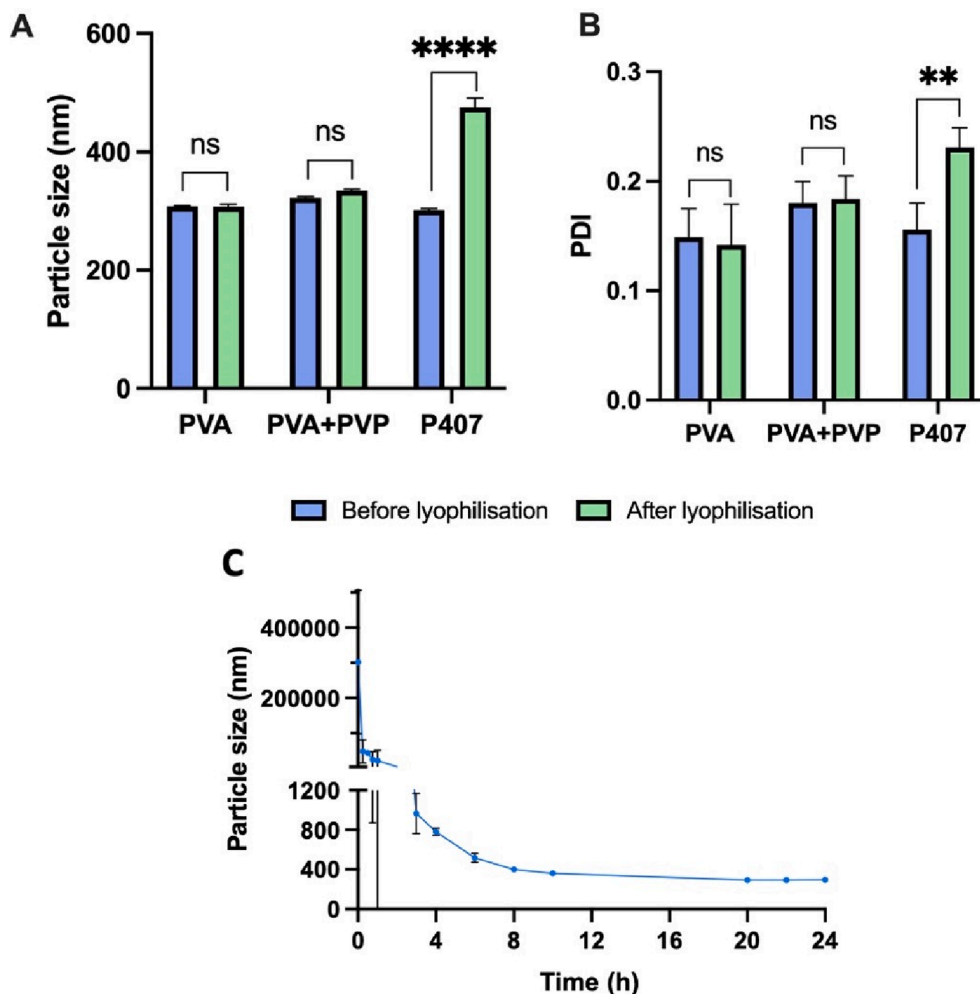
Fig. 1. (A) NCs particle size and (B) PDI before and after lyophilisation for NCs stabilised by PVA, PVA and PVP and P407 (Means + SD, n = 3). (C) The effect of milling time on NCs particle size (Means ± SD, n = 3).

lyophilisation. Regarding the PDI (Fig. 1**B**), which was measured before lyophilization, no significant difference was found between the NC ($p >$ 0.05) samples produced using PVA, PVA:PVP, or P407 as stabilizer solutions. After lyophilisation, NCs stabilized by PVA solution showed a significantly lower ($p < 0.05$) PDI than those prepared with P407. This could be because of the ability of PVA not only to be adsorbed on the surface of the particle but also to form a glassy matrix around NCs during freezing which lead to an enhanced stability in terms of particle size and PDI (Abdelwahed et al., 2006). However, the PDI of NCs stabilized by PVA or PVA:PVP solutions did not show a significant difference ($p >$ 0.05), as shown in Fig. 1**B**. Therefore, the final formulation selected consisted of 300 mg of RIS, 4 magnetic stirrers (12 x 6 mm), 2 mL ceramic beads (0.1–0.2 mm), and 6 mL of 2 % w/w PVA 9–10 kDa solution, all placed together in a 7.5 mL glass vial. As displayed in Fig. 1**C,** the milling time of RIS particles were found to be in the micron size range for the first 4 h. Consistently sized nanoparticles were achieved after 20 h. After 20 h, no significant reduction ($p > 0.05$) in particle size was observed with increasing milling time.

3.2. Characterisation of risperidone nanocrystals

The actual amount of drug in each 100 mg sample of lyophilised NCs was determined, and the percentage of drug in the NCs formulation was calculated and compared with the theoretical drug content percentage to evaluate the amount of drug lost during the NCs production process. The actual content of RIS in lyophilised NCs (n = 9) was found to be 0.71 ± 0.04 mg, equivalent to 71.1 % per 100 mg of nanocrystals. Furthermore, based on the theoretical drug content, considering the amount of PVA (300 mg) and RIS (120 mg) involved in the preparation of NCs, it was calculated to be 71.42 % of drug, confirming the efficiency of the nanocrystallization process. As shown in Fig. 2**A**, bulk RIS exhibited a wide range of particle sizes and various shapes. In contrast, the lyophilized NCs powder was more uniform in terms of particle size and shape. Additionally, the surface of the lyophilized samples appeared more porous compared to bulk RIS, which is expected due to the removal of water through freeze-drying (Qian and Zhang, 2011).

The FTIR spectra of RIS, PVA 9–10 KDa, PM and NCs are shown in Fig. 2**B**. FTIR was used to identify any chemical interactions between RIS
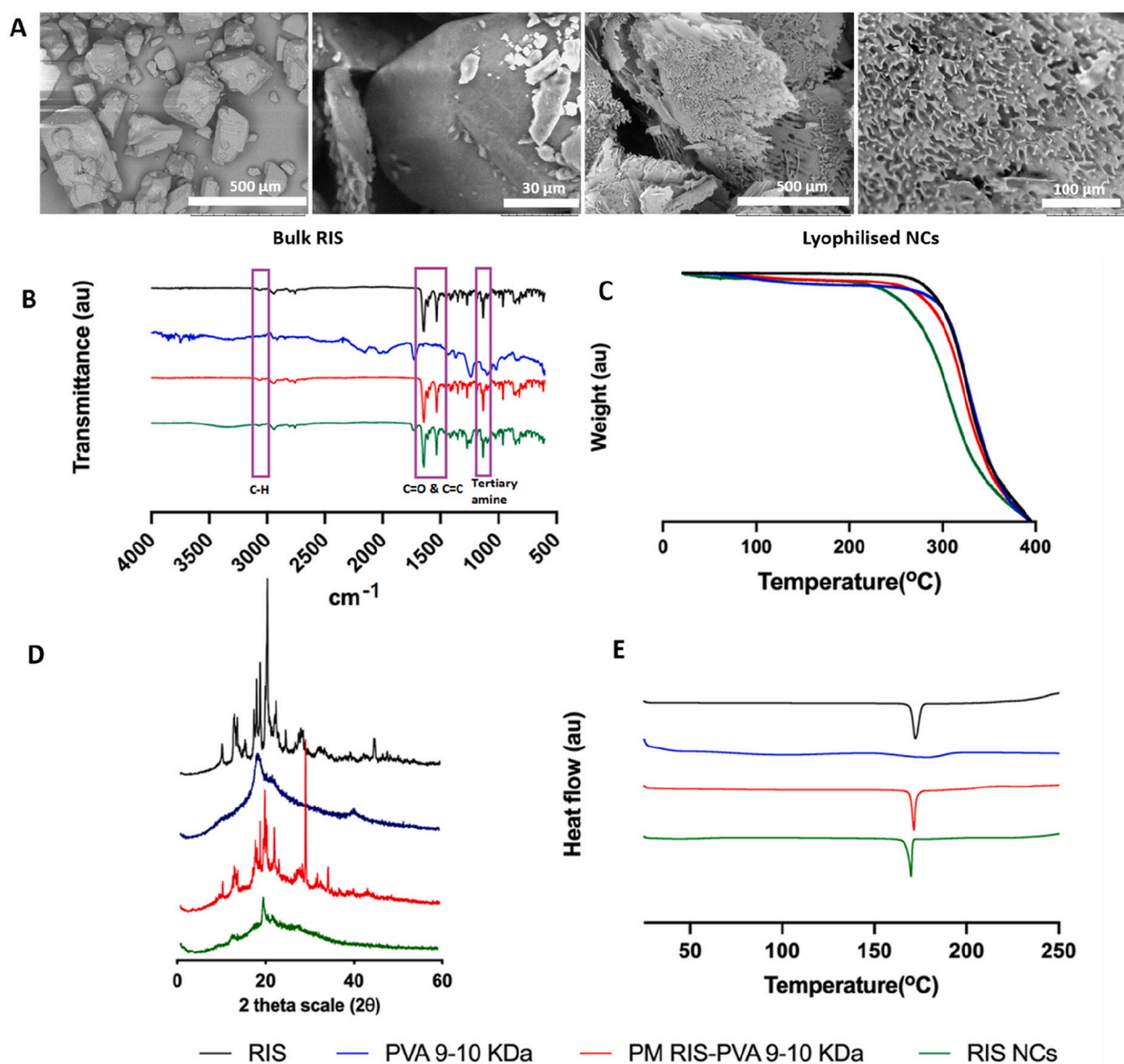

Fig. 2. (A) SEM images for bulk RIS and lyophilised NCs. (B) FTIR spectra, (C) TGA analysis, (D) DSC thermogram, (E) XRD diffractogram of RIS, PVA 9–10 KDa, PM and NCs.

and PVA through the analysis of the fundamental molecular vibration. In the RIS spectra, a weak band appeared at 3068 cm^{-1}, corresponding to the C-H stretching of the aromatic ring. A band at 1651 cm^{-1} was attributed to the C $=$ O bond of the δ-lactam ring. Additionally, other peaks were detected at 1610 cm^{-1} and 1536 cm^{-1}, indicating the C $=$ C stretching of the aromatic ring. Weak peaks around 1400 cm^{-1} were noticed, corresponding to C-N and C-O angular deformations of the oxazole ring. An intermediate band of C-N stretching in the oxazole ring was observed at 1350 cm^{-1}. Furthermore, another intermediate band corresponding to the tertiary amine of the piperidine ring was detected at 1194 cm^{-1}. Lastly, a strong band at 1131 cm^{-1} was attributed to the aryl fluoride (Utomo et al., 2022). The FTIR spectrum of PVA revealed a broad peak between 3500 cm^{-1} and 3200 cm^{-1}, corresponding to O-H from the intermolecular and intramolecular hydrogen bonds. A vibration band at 2920 cm^{-1} was noticed due to C-H stretching. The stretching vibrational band of C $=$ O at 1730 cm^{-1} is attributed to the carbonyl functional groups (Mansur et al., 2008; Korbag and Mohamed Saleh, 2016). The characteristics of RIS spectra were retained in the spectra obtained by analysing the respective PM and NCs, and no new peaks emerged. This indicates that no new bond has formed during the milling of RIS to form NCs.

The purpose of conducting the TGA was twofold: to examine any changes in terms of drug degradation following the formation of NCs, and to assess the efficacy of the freeze-drying method in removing water from the NCs samples, as presented in Fig. 2C. In the case of pure RIS, a significant mass loss commenced at 240 °C, depicted by a steep curve, which corresponds to the decomposition of RIS (Daniel et al., 2013). A similar trend was observed in the thermograms of the PM and NCs, with the NCs exhibiting an earlier onset due to their smaller particle size and higher surface energy, resulting in lower thermal stability (Quan et al., 2021). Regarding water loss, both PVA and PVA-containing formulations displayed initial minor weight loss up to 100 °C. The total water content of RIS NCs was determined to be 1.26 %, indicating the effectiveness of the freeze-drying process in removing water.

PXRD was utilised to assess the crystallinity of the formulations, as depicted in Fig. 2D. The distinct peaks observed in the pure RIS PXRD patterns confirm the crystalline nature of RIS. The diffractogram of RIS exhibited sharp peaks at 2-theta values of 12.1°, 14.78°, 19.7°, 20.46°, 22.04°, 23.94°, 26.06°, and 45.42° (Bera et al., 2015). On the other hand, PVA 9–10 KDa did not exhibit clear peaks due to the amorphous characteristics of this polymer. However, its diffractogram displayed an increase in the diffraction pattern at 20° and 40.94°. In the PM, all the characteristic peaks were retained at nearly the same (2θ) angles. The diffractogram of the NCs displayed the main peaks observed in the pure RIS diffractogram but with lower intensity, possibly due to the presence of the amorphous polymer as the peak height is affected by crystal size and crystallinity (Kayal and Ramanujan, 2010; Koradia et al., 2018). Additionally, the reduction in particle size resulted in broadening of the PXRD peaks. Moreover, variations in particle morphology could lead to changes in the PXRD diffractograms (Holder and Schaak, 2019). This suggests that no significant phase changes or chemical reactions occurred between RIS and PVA during the wet media milling process. To validate the XRD results, DSC analysis was conducted (Fig. 2E). Pure RIS exhibited an endothermic peak at 172.24 °C, corresponding to the reported melting point of the drug in previous studies as 171.1 °C (Utomo et al., 2022). The melting peak of RIS was also observed in the DSC thermograms of both the PM and NCs, confirming the absence of any chemical interactions between RIS and PVA. Furthermore, it affirms that the crystalline nature of RIS was unaffected during the milling process. The slight shift in the endothermic peak of RIS in the NCs formulation to 169.96 °C might be attributed to the smaller size of RIS crystals (Van Eerdenbrugh et al., 2008).

3.3. In vitro release study

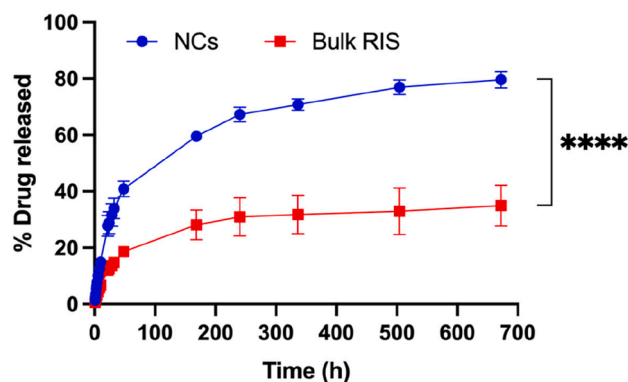*In vitro* release profile of bulk RIS and RIS NCs are depicted in Fig. 3.

Fig. 3. *In vitro* release of bulk RIS and NCs through dialysis membranes in 1 % SLS in PBS (pH 7.4) at 37 °C in an orbital shaker at 100 rpm (Means ± SD, n = 3).

The findings indicate a substantial improvement in the release percentage of RIS, reaching up to 80 %, by formulating the drug as NCs compared to 35 % released from bulk RIS over 28 days (p < 0.0001). This enhancement can be attributed to the smaller particle size of the NCs, resulting in a higher surface area that contributes to an increased dissolution rate and solubility (McGuckin et al., 2022; Mauludin et al., 2009).

3.4. Fabrication of dissolving MAP

Digital images for bulk RIS and RIS loaded MAPs are shown in Fig. 4A. The fabrication process for MAPs with a PVP (360 KDa) baseplate yielded well-formed MAPs devoid of bubbles. In the case of NCs-loaded MAPs, it was observed that the drug was primarily concentrated at the tips rather than uniformly distributed throughout the entire matrix, as seen in bulk RIS MAPs. This can be attributed to the small nano-sized particles of RIS, which enable them to reach the narrow tips of the MAP projections. The percentage of bulk drug and the amount of water added to reconstitute the lyophilised NCs were rationalised for bulk drug-loaded MAPs and NCs-loaded MAPs, respectively. This rationalisation was necessary to achieve a mixture that is sufficiently liquid to be spread evenly over the moulds, yet viscous enough to facilitate the removal of excess formulation and achieve high drug loading in the MAPs. PVA was utilised not only as a stabiliser for NCs but also as a matrix for MAPs. This allowed for a simple fabrication procedure without the need for additional excipients. In the case of bulk drug-loaded MAPs, PVA and PVP were combined due to their advantageous characteristics reported in previous studies on dissolving MAP manufacturing. Both polymers are water-soluble and biocompatible (Zhang et al., 2021). Previous research has demonstrated that combining PVA and PVP capitalises on the mechanical strength of PVA and the high hydrophilicity of PVP (Lilleby Helberg et al., 2020). Specifically, dissolving MAPs fabricated using a blend of PVA and PVP exhibited superior mechanical properties compared to using either polymer alone. This may be attributed to the formation of hydrogen bonds between the (C $=$ O) groups of PVP and the (OH) groups of PVA (Permana et al., 2019). Both PVA and PVP were used in low molecular weights as they can be eliminated by the kidneys, thus avoiding accumulation in the body (Ruggiero et al., 2010). This is particularly important as the treatment of schizophrenia will necessitate repeated use of MAPs over an extended period, and the build-up of excipients should be avoided. All MAPs were cast using a two-step approach, with the active ingredient incorporated solely in the tips of the MAPs. This technique offers several advantages. Firstly, it minimises drug wastage, especially for hydrophobic drugs that are unlikely to permeate from the baseplate of the MAPs. Secondly, the presence of the drug in both layers (tips and baseplate) would compromise the mechanical properties
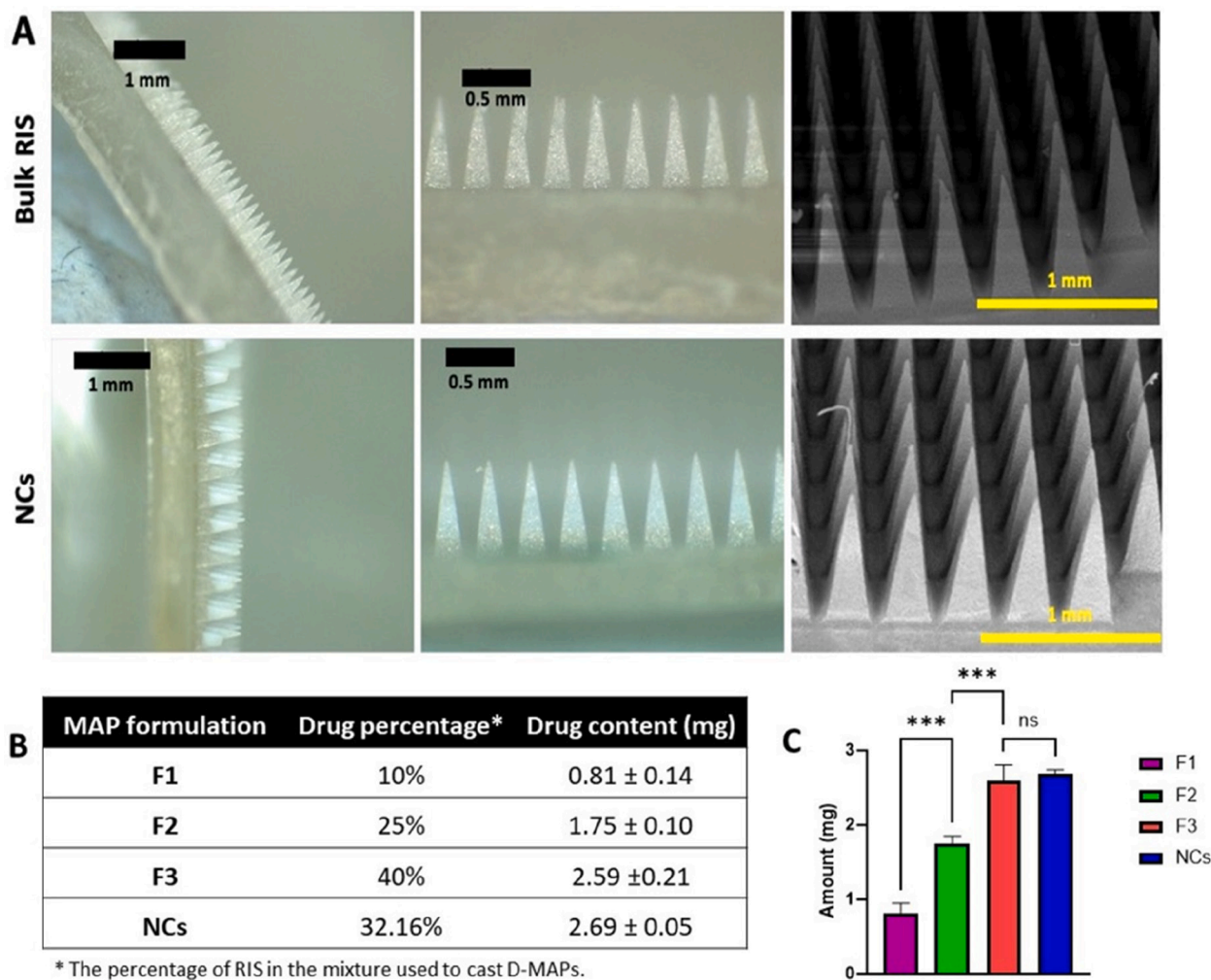
Fig. 4. (A) Digital microscopic and SEM images for bulk RIS loaded MAPs and NCs loaded MAPs. (B) The theoretical and experimental drug content in different formulations of dissolving MAPs (Means ± SD, n = 3). (C) Drug content in different dissolving MAP formulations (Means + SD, n = 3).

compared to MAPs containing the drug only in the tips. Lastly, this approach is more conducive to industrial-scale production (Permana et al., 2020).

3.5. Drug loading of dissolving MAPs

As can be seen in Fig. 4**B** and **4C**, increasing the percentage of drug in the mixture that was cast into MAPs resulted in higher actual drug content. Further studies compared MAPs containing 40 % bulk RIS with NCs-loaded MAPs, as these two formulations showed no significant difference ($p > 0.05$) in the actual drug content. Therefore, F3 was selected for further study to ensure a fair comparison in terms of drug permeation study in the *ex vivo* studies compared to MAP containing NCs.

3.6. Evaluation of mechanical characteristics and insertion properties of dissolving MAPs

Strength evaluation of individual MNs in the four MAPs formulations was performed by conducting a compression test and measuring the percentage of height reduction. This test was also performed to ensure that the needles would withstand pressure and not break when applied to the skin. As shown in Fig. 5**A**, the percentage height reduction of F1, F2, F3, and NCs-loaded MAPs was 12.18 %, 17.29 %, 27.51 %, and 10.74 %, respectively. Comparing the two formulations, F3 and NCs-

loaded MAPs, with the latter containing the highest amount of drug, it was clearly evident that NCs-loaded MAPs were more robust and could handle more pressure than F3 MAPs. This could be attributed to the homogeneity of the particles that formed the needles.

As illustrated in Fig. 5**B**, all MAP formulations penetrated through the first and second layers of Parafilm® M to 100 %. Additionally, all formulations reached the fourth layer of Parafilm® M. Considering that the mean thickness of each layer is approximately 126 μm, this suggests that all MAPs were inserted to a minimum depth of 504 μm, corresponding to 67.2 % of the MN height. This insertion depth indicates that the needles might penetrate the *stratum corneum* and epidermis layers to further reach the upper layer of the dermis and release the cargo into the microcirculation (Anjani et al., 2022; Anjani et al., 2022; Anjani et al., 2023). Despite the significant difference in height reduction between MAPs of F3 and NCs ($p < 0.0001$) (Fig. 5**A**), the insertion profiles of these two formulations showed no significant difference ($p > 0.05$). The mechanical resistance of MAPs was evaluated by measuring the reduction in needle height before and after compression, with the needles in direct contact with a flat metal surface. These results demonstrate how the MAPs resist axial force against a solid structure. However, in the context of insertion studies, the MAPs were inserted into a stack of Parafilm® M layers, a validated skin simulant for this purpose, which is more flexible than a metal flat surface, thus yielding different results. These findings are consistent with previously published results (Anjani et al., 2022; Anjani et al., 2022; Anjani et al., 2023). The insertion depths
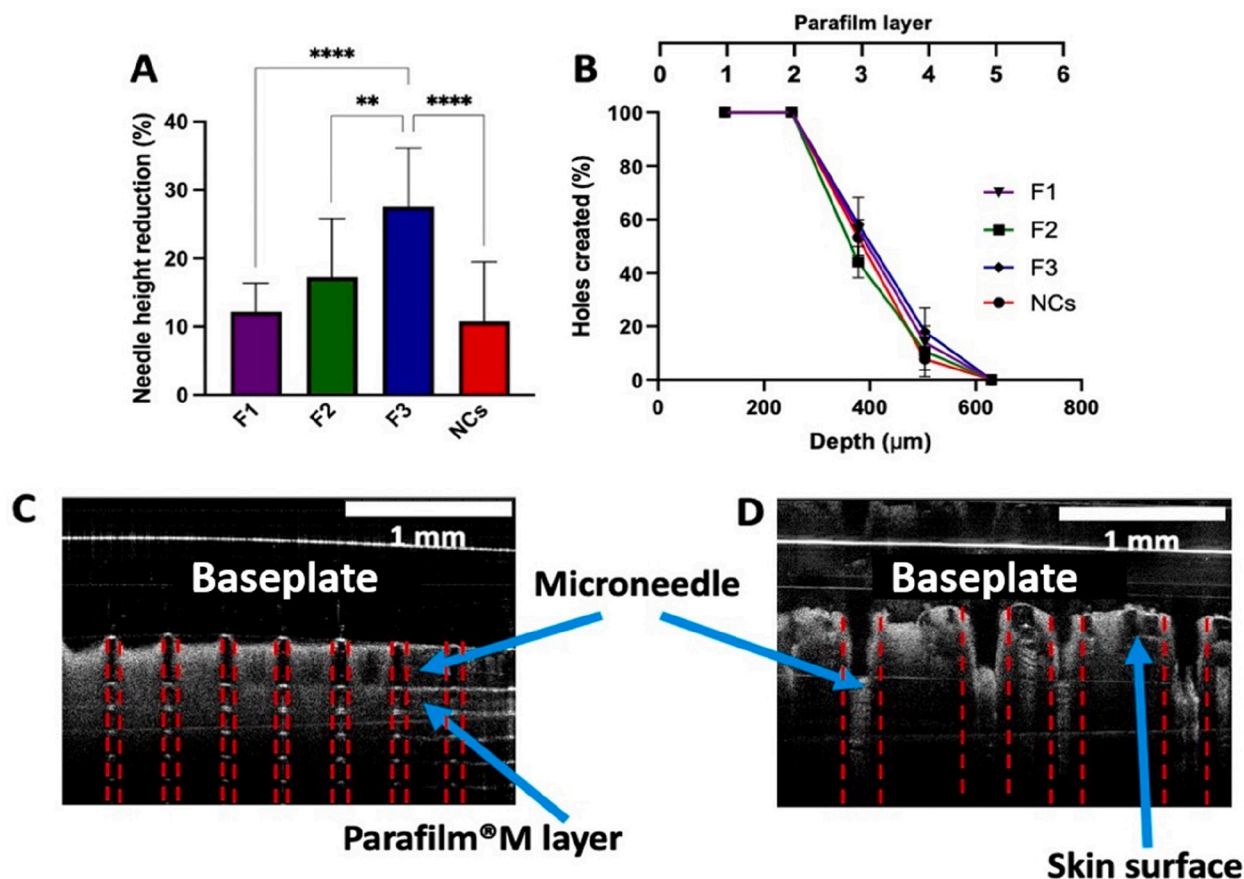
Fig. 5. (A) Percentage of needle height reduction after applying a force of 32 N for 30 sec (Means + SD, n = 60). (B) Insertion efficiency of different formulations of dissolving MAPs into eight layers of Parafilm® M (Means ± SD, n = 3). (C) OCT image for NCs loaded DMAPs inserted in Parafilm® M. (D) OCT image for NCs loaded DMAPs inserted in full-thickness neonatal porcine skin.

were visualized *in vitro* and *ex vivo* skin models using OCT, as shown in Fig. 5C and 5D. MAPs displayed an insertion depth of 451.47 ± 5.63 and 595.58 ± 28.16 μm in Parafilm® M and skin, respectively. The gap between the baseplate and both the first layer of the Parafilm® M and the full-thickness neonatal porcine skin is due to the incomplete insertion of the MAPs which is comparable with the results of the Parafilm® M insertion test results shown in Fig. 5B.

3.7. Ex vivo permeation and skin deposition studies

Franz diffusion cells were employed to measure drug delivery to the receiver compartment and the amount deposited in the skin. The permeation profiles of DMAPs loaded with 40 % bulk RIS and RIS NCs were compared and presented in Fig. 6A. The permeation profiles at predetermined time points for each type of dissolving MAPs indicated that there was no significant difference in RIS release from DMAPs
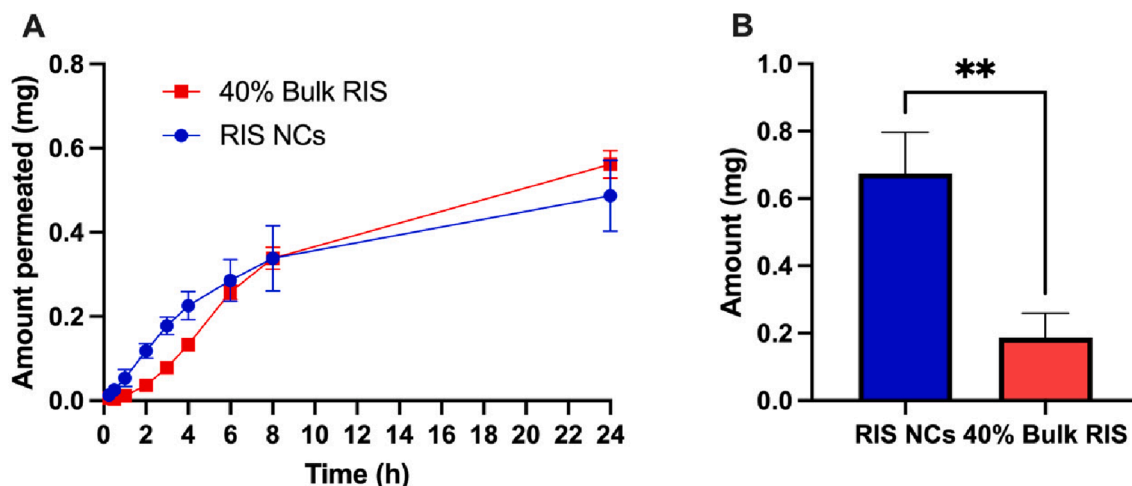

Fig. 6. (A) Amount of RIS permeated across the neonatal porcine full-thickness skin over 24 h from dissolving MAPs (Means ± SD, n = 3). (B) Amount of RIS deposited in the skin after 24 h (Means + SD, n = 3).

containing 40 % bulk RIS and DMAPs containing NCs at 24 h ($p > 0.05$). However, the amount of RIS deposited in the full thickness of the skin after 24 h (Fig. 6**B**) was significantly higher for NCs-loaded MAPs ($p < 0.05$). This could be due to the smaller particle size that allows the drug to reach the narrow region of tips of the MAPs allowing more drug to deposit in the skin, while more drug would potentially be in the upper region of bulk drug loaded MAPs. Since the needles do not insert 100 % of their length into skin, this drug is then undelivered. These findings suggest the potential for long-acting effects of RIS when NCs-loaded MAPs are applied.

After 24 h of application, and based on a calculated extraction recovery percentage of 97.89 %, the amount of RIS permeated across the full thickness of neonatal porcine skin from NCs-loaded MAPs and 40 % bulk RIS was approximately 0.49 ± 0.08 mg and 0.56 ± 0.03 mg, respectively. Meanwhile, the amount of drug deposited in the skin from these two formulations was 0.67 ± 0.12 mg and 0.19 ± 0.07 mg, respectively. In total, approximately 1.16 mg of RIS was released from the NCs-loaded DMAPs, while only approximately 0.75 mg of RIS was released from bulk-loaded DMAPs. When viewed as a percentage of drug delivery efficiency, NCs-loaded DMAPs exhibited higher efficiency (42.96 %) of RIS delivery into and across the skin compared to bulk-loaded DMAPs (28.84 %). The higher delivery efficiency of NCs-loaded MAPs could be attributed to the drug's availability in the tips of the MAPs, as NCs are smaller in size compared to bulk drug and can reach the narrow parts of the needles more effectively. Larger particles, on the other hand, have a higher chance of being distributed along the entire length of the MAPs. Additionally, studies by Fereig *et al.* on Tacrolimus-loaded chitosan nanoparticles have reported that particles in the nano-size range enhance the amount of drug deposition in the skin layers compared to larger particles (Fereig et al., 2021). As elucidated by Mauludin *et al.,* drug particles with nanometer-sized dimensions have a significantly larger specific surface area, as well as higher particle curvature, which increases the dissolution pressure and leads to a greater amount of dissolved molecules available for absorption (Mauludin et al., 2009).

3.8. Biocompatibility studies

To assess the potential applicability of the formulations on the skin, cytotoxicity studies were conducted using human dermal fibroblasts (HDFa) cells. Initially, the MTT assay was employed to evaluate the impact of the formulations on cell viability. As depicted in Fig. 7**A**, the blank formulation exhibited no effect on cell viability after 48 h, similar to the control cells. However, the MAP loaded formulation led to a reduction in cell viability (93.14 %) compared to the control (p < 0.05). These results suggest that the MN loaded formulation affected skin cells, resulting in lower cell viability in the experiment at a non-cytotoxic level (grade 1), as per the cytotoxicity grade levels described previously (Li et al., 2015). The observation that RIS increased the toxicity level based on the concentration used aligns with previously reported study (Zheng et al., 2019).

In this context, a rise in RIS concentration resulted in a decrease in the percentage of viable cells at a mild level. Consequently, the obtained outcomes indicate that the formulations were non-toxic to human dermal cells. Despite the RIS-loaded MAP displaying a decrease in viable cells, the measured values were still categorised as lacking toxicity. To provide a more comprehensive understanding of the cell numbers within the well plates, the picogreen assay was executed to determine the total DNA concentration in the medium. This is a reliable indicator of cell numbers and proliferation. Illustrated in Fig. 7**B**, the samples exhibited a slight reduction in HDFa cell proliferation after MN loaded sample exposure compared to the control. This finding aligns with the viability results, suggesting that RIS also influenced cell proliferation with a slight reduction. This effect is primarily due to the altered cell viability numbers, as previously described in fibroblast studies (Zheng et al., 2019). Furthermore, the compatibility of the formulations with cells was confirmed through the live-dead assay (Fig. 7**C**), which revealed minimal cell death after two days of cell culture. In summary, the collective evidence underscores the good cytocompatibility of the formulations, positioning them as promising materials for potential use on the skin.
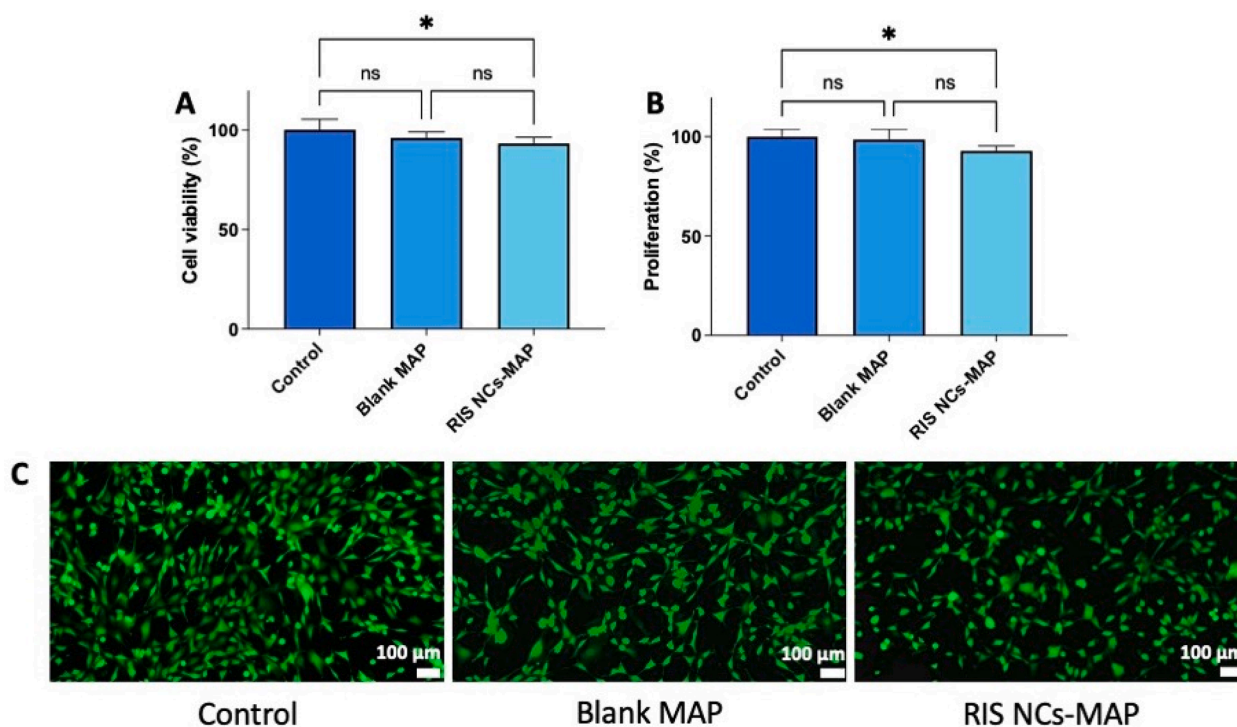

Fig. 7. Cytotoxicity Study. (A) MTT assay at 48 h, leaching solutions of the formulations and positive control were exposed to cells with media (Means + SD, n = 5). (B) Percentage of DNA concentration shown by the picogreen assay (Means + SD, n = 5). (C) Microphotographs of treated cells following the live-dead assay (scale bar 100 μm) with positive control (n = 5).

3.9. *In vivo and pharmacokinetic studies*

In vivo study was conducted to evaluate the drug delivery of RIS transdermally through the application of NCs loaded MAPs. Female Sprague Dawley rats had MAPs manually applied into their backs, where they were kept for 24 h, while the study continued for 14 days (336 h). After 24 h, the kinesiology and Microfoam™ adhesive tapes were removed. Those tapes were used to ensure the good adhesion of the MAPs onto the skin that plays a vital role in the efficiency of drug delivery and subsequently the therapeutic effects (Banerjee et al., 2014). After skin observation, tips were completely inserted into rats' skin and separated from the baseplates and a polymer residual was left on the skin due to the dissolving of the baseplate (Fig. 8**A**). A noticeable implantation of the dissolving tips containing RIS (white in colour) was observed especially after cleaning the skin (Fig. 8**B**).

The *in vivo* plasma profiles of RIS and 9-OH-RIS were obtained after the administration of 17 mg/kg RIS both orally and through DMAPs as presented in Fig. 9. The dose was determined based on the drug content in DMAPs and the conversion of the maximum oral human dose into rat's oral dose along with the results from a published study where rats received an oral dose of 30 mg/kg with no reports of toxic reactions or side effects (Nair and Jacob, 2016; Gu et al., 2016). Also, RIS and 9-OH-RIS pharmacokinetic parameters were assessed after applying MAPs and compared with the same parameters after the oral administration of RIS suspension as shown in Table 1.

For oral control group, an immediate increase in RIS plasma levels was noticed with C_{max} of 157.38 ± 107.62 ng/mL at t = 1 h (T_{max}). After four hours, the plasma levels declined quickly and RIS was not detected at t = 24 h. Similar trend was seen for plasma levels of 9-OH-RIS with a shift of the T_{max} to t = 4 h and about ten folds higher C_{max} of 1600.11 ± 435.95 ng/mL. 9-OH-RIS appeared as the major metabolite in blood circulation after the administration of RIS (Lu et al., 2008). The quick elimination of RIS and its metabolite after the oral administration was expected, as frequent dosing is needed for the oral dosage form of RIS (McNeil et al., 2022). The plasma concentration of RIS in rats that received the NCs loaded MAPs increased to reach 554.84 ± 61.82 ng/

mL (C_{max}) in the first hour. After that, plasma levels decreased, but were detectable until day 5. Afterwards, plasma levels were below the lower limit of quantification of the validated bioanalytical method (10 ng/mL). Moreover, plasma levels of 9-OH-RIS increased gradually to reach the maximum of 324.13 ± 27.86 ng/mL at t = 4 h (T_{max}). Then a nonsignificant decline of 9-OH-RIS concentration occurred until 24 h. After 24 h, plasma levels of 9-OH-RIS gradually decreased to reach 6.74 ± 8.26 ng/mL on day 5, after which 9-OH-RIS was not detectable or below the limit of quantification (1 ng/mL). Due to the metabolism of RIS by CYP450, specifically CYP2D6 in the liver, 9-OH-RIS levels were higher for the oral group compared to the MAPs group in which the drug would be firstly permeated through the skin into the systemic circulation before its ultimate hydroxylation in the liver (Fang et al., 1999). This also confirms the delay in reaching the C_{max} (extended T_{max}).

Furthermore, compared to the oral control, the extended release of RIS from the MAPs produced systemic exposure levels that were around 15 times higher. Significantly ($p < 0.0001$) higher AUC_{0-t} of 491.7 ± 47.90 ng/ml*h were obtained from MAPs group compared to 32.44 ± 8.66 ng/ml*h from oral group. Furthermore, MAPs attained MRT values of 26.70 ± 8.62 h, which were significantly ($p = 0.0107$) higher than MRT values of 4.10 ± 0.97 h from oral administration. The prolonged MRT may be caused by the sustained release of RIS from MAPs formulation (Weng et al., 2016). On the other hand, although 9-OH-RIS was detected in the plasma for longer time from the MAPs formulation compared to the oral dose, there was no significant difference ($p = 0.077$) in the AUC_{0-t}. This could be due to the dramatic increase in plasma levels of 9-OH-RIS after oral administration due to the hepatic metabolism of RIS to its active metabolite. The MRT for 9-OH-RIS was extended to 30.94 ± 12.84 h in the MAPs group compared to 4.83 ± 0.59 h after oral administration.

Based on the oral bioavailability of nearly 70 % as mentioned in the literature, the relative bioavailability RIS delivered by DMAPs was calculated to be 4.93 % (Serretti, 2024). This value equates to approximately 0.53 mg RIS delivered transdermally to rats in the DMAPs group over 5 days. As the optimum therapeutic oral daily dose of RIS which is 4 – 8 mg/day and the oral bioavailability is 70 %, approximately 2.8 – 5.6
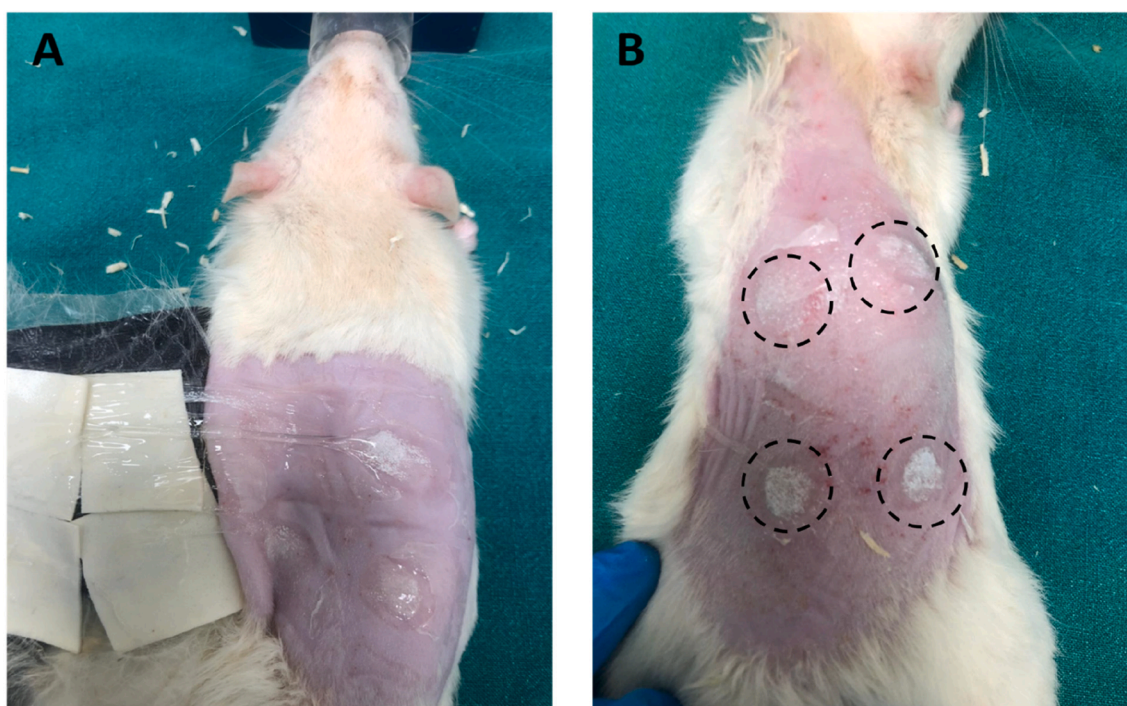
Fig. 8. Digital images taken immediately after DMAPs removal (24 h following their application). (A) The dorsal area with the MNs separated from the baseplate. (B) The dorsal area after cleaning polymer residues showing drug deposition in the skin (The white areas within the black circles).
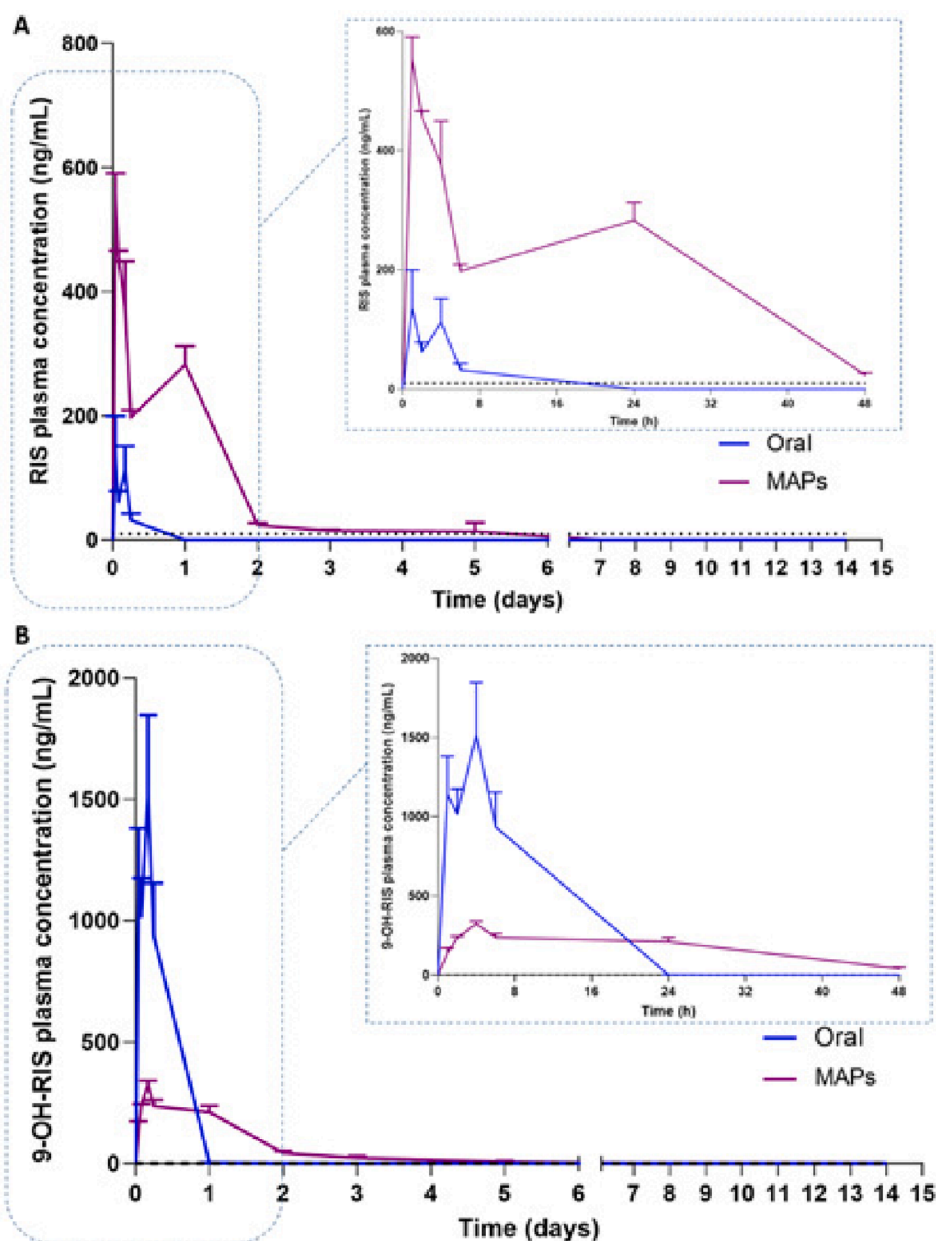
Fig. 9. Plasma levels of (A) RIS and (B) 9-OH-RIS after the administration of a dose of RIS equivalent to 5 mg (17 mg/kg) by oral gavage and the application of four NCs loaded DMAPs after the 14-day *in vivo* study for (Means + SD, n = 6 at 1, 2, 4 and 6 h, n = 12 at the remaining time points). The black dashed line represents the LLOQ of the analytical method (10 ng/mL for RIS and 1 ng/mL for 9-OH-RIS).

Table 1

In vivo plasma pharmacokinetic parameters of RIS after oral and DMAPs administration to Sprague–Dawley rats (Means ± SD, n = 6 for each group).

Parameter	RIS		9-OH-RIS	
	Oral	**MAPs**	**Oral**	**MAPs**
T_{max} (h)	1	1	4	4
C_{max} (ng/mL)	157.38 ± 107.62	554.84 ± 61.82	1600.11 ± 435.95	324.13 ± 27.86
AUC_{0-t} (ng/ mL*h)	777.2 ± 207.6	11789 ± 1149	15105.59 ± 3522.91	10124 ± 932.4
MRT (h)	4.10 ± 0.97	26.70 ± 8.62	4.83 ± 0.59	30.94 ± 12.84

mg should be delivered transdermally using DMAPs. To achieve this, and given that the amount of RIS delivered from 4 MAPs with a total area of 3 cm^2 was 0.53 mg, a patch size of 15.85 – 31.70 cm^2 could potentially yield therapeutically relevant concentrations in humans. Consequently, a patch size of 79.25 – 158.5 cm2 would be needed to deliver therapeutically relevant plasma concentrations of RIS over 5 days from a single application for 24 h.

4. Conclusion

This work described, for the first time, the development of bulk RIS and RIS NCs loaded DMAPs for the purpose of enhancing transdermal delivery of RIS. Bulk drug loaded DMAPs were easily prepared by mixing the drug in a specific ratio with PVA (9–10 KDa) and PVP (58 KDa) gel mixture. For NCs loaded MAPs, a simple laboratory-scaled wet media-milling strategy was employed to produce NCs that were then casted

as MNs using previously fabricated moulds in a simple way by only adding deionized water. This resulted in NCs with particles that had a diameter around 300 nm. All formulations were tested for their drug content, mechanical and insertion properties and *ex vivo* drug permeation and skin deposition. When tested *in vivo*, RIS and its metabolite 9-OH-RIS were detected in plasma samples for up to 5 days in rats received NCs loaded DMAPs. Furthermore, the work presented here offers an alternative delivery route for RIS capable of achieving therapeutic doses, associated with less dosing frequency, for a prolonged period of time. However, addressing the challenges related to manufacturing, skin variability, regulatory hurdles, drug formulation, and patient acceptance is crucial for their successful clinical implementation. Future work should focus on the optimization of drug loading and to do pharmacodynamics studies in suitable animal models.

CRediT authorship contribution statement

Rand Ghanma: Writing – review & editing, Writing – original draft, Methodology, Investigation, Formal analysis, Data curation, Conceptualization. **Yara A. Naser:** Methodology, Investigation, Formal analysis. **Qonita Kurnia Anjani:** Writing – review & editing, Writing – original draft, Visualization. **Akmal Hidayat Bin Sabri:** Investigation, Formal analysis. **Aaron R.J. Hutton:** Investigation, Formal analysis. **Lalitkumar K. Vora:** Investigation, Formal analysis. **Achmad Himawan:** Formal analysis, Data curation. **Natalia Moreno-Castellanos:** Methodology, Formal analysis, Data curation. **Brett Greer:** Resources, Formal analysis. **Helen O. McCarthy:** Resources. **Alejandro J. Paredes:** Supervision, Methodology, Formal analysis. **Ryan F. Donnelly:** Writing – review & editing, Supervision, Resources, Methodology, Funding acquisition, Formal analysis, Conceptualization.

Declaration of competing interest

The authors declare that they have no known competing financial interests or personal relationships that could have appeared to influence the work reported in this paper.

Data availability

Data will be made available on request.

Acknowledgments

References

S. Abdelghany, I.A. Tekko, L. Vora, E. Larrañeta, A.D. Permana, R.F. Donnelly, Nanosuspension-Based Dissolving Microneedle Arrays for Intradermal Delivery of Curcumin, Pharmaceutics 2019, Vol. 11, Page 308 11 (2019) 308. DOI: 10.3390/PHARMACEUTICS11070308.

Abdelwahed, W., Degobert, G., Stainmesse, S., Fessi, H., 2006. Freeze-drying of nanoparticles: Formulation, process and storage considerations. Adv Drug Deliv Rev 58, 1688–1713. https://doi.org/10.1016/J.ADDR.2006.09.017.

Al-Akayleh, F., Adwan, S., Khanfar, M., Idkaidek, N., Al-Remawi, M., 2020. A novel eutectic-based transdermal delivery system for risperidone. American Association of Pharmaceutical Scientists 22, 4. https://doi.org/10.1208/s12249-020-01844-4.

Altuntaş, E., Tekko, I.A., Vora, L.K., Kumar, N., Brodsky, R., Chevallier, O., McAlister, E., Kurnia Anjani, Q., McCarthy, H.O., Donnelly, R.F., 2022. Nestorone nanosuspension-loaded dissolving microneedles array patch: A promising novel approach for "on-demand" hormonal female-controlled peritcoital contraception. Int J Pharm 614, 121422. https://doi.org/10.1016/J.IJPHARM.2021.121422.

Anjani, Q.K., Bin Sabri, A.H., Hamid, K.A., Moreno-Castellanos, N., Li, H., Donnelly, R.F., 2023. Tip loaded cyclodextrin-carvedilol complexes microarray patches. Carbohydr Polym 320, 121194.

Q.K. Anjani, J. Domínguez-Robles, E. Utomo, M. Font, M.C. Martínez-Ohárriz, A.D. Permana, Á. Cárcamo-Martínez, E. Larrañeta, R.F. Donnelly, Inclusion Complexes of Rifampicin with Native and Derivatized Cyclodextrins: In Silico Modeling, Formulation, and Characterization, Pharmaceuticals (Basel) 15 (2021). DOI: 10.3390/PH15010020.

Q.K. Anjani, A.H. Bin Sabri, M.B. McGuckin, H. Li, K.A. Hamid, R.F. Donnelly, In Vitro Permeation Studies on Carvedilol Containing Dissolving Microarray Patches Quantified Using a Rapid and Simple HPLC-UV Analytical Method, AAPS PharmSciTech 23 (2022) 1–13. DOI: 10.1208/S12249-022-02422-6/FIGURES/4.

Q.K. Anjani, Á. Cárcamo-Martínez, L.A.H. Wardoyo, N. Moreno-Castellanos, A.H. Bin Sabri, E. Larrañeta, R.F. Donnelly, MAP-box: a novel, low-cost and easy-to-fabricate 3D-printed box for the storage and transportation of dissolving microneedle array patches, Drug Deliv Transl Res (2023). DOI: 10.1007/s13346-023-01393-w.

Anjani, Q.K., Permana, A.D., Cárcamo-Martínez, Á., Domínguez-Robles, J., Tekko, I.A., Larrañeta, E., Vora, L.K., Ramadon, D., Donnelly, R.F., 2021. Versatility of hydrogel-forming microneedles in in vitro transdermal delivery of tuberculosis drugs. Eur. J. Pharm. Biopharm. 294–312, 294–312. https://doi.org/10.1016/j.ejpb.2020.12.003.

Anjani, Q.K., Bin Sabri, A.H., Utomo, E., Domínguez-Robles, J., Donnelly, R.F., 2022. Elucidating the Impact of Surfactants on the Performance of Dissolving Microneedle Array Patches. Mol Pharm 19, 1191–1208. https://doi.org/10.1021/ACS.MOLPHARMACEUT.1C00988/ASSET/IMAGES/LARGE/MP1C00988_0014.JPEG.

Anjani, Q.K., Bin Sabri, A.H., Domínguez-Robles, J., Moreno-Castellanos, N., Utomo, E., Wardoyo, L.A.H., Larrañeta, E., Donnelly, R.F., 2022. Metronidazole nanosuspension loaded dissolving microarray patches: An engineered composite pharmaceutical system for the treatment of skin and soft tissue infection. Biomaterials Advances 140, 213073. https://doi.org/10.1016/J.BIOADV.2022.213073.

Anjani, Q.K., Hidayat, A., Sabri, B., Moreno-Castellanos, N., Utomo, E., Cárcamo-Martínez, Á., Domínguez-Robles, J., Ahmadi, L., Wardoyo, H., Donnelly, R.F., 2022. Soluplus®-based dissolving microarray patches loaded with colchicine: towards a minimally invasive treatment and management of gout. Biomater Sci. https://doi.org/10.1039/D2BM01068B.

Anjani, Q.K., Pandya, A.K., Demartis, S., Domínguez-Robles, J., Moreno-Castellanos, N., Li, H., Gavini, E., Patravale, V.B., Donnelly, R.F., 2023. Liposome-loaded polymeric microneedles for enhanced skin deposition of rifampicin. Int J Pharm 646, 123446. https://doi.org/10.1016/J.IJPHARM.2023.123446.

Anjani, Q.K., Volpe-Zanutto, F., Hamid, K.A., Bin Sabri, A.H., Moreno-Castellano, N., Gaitán, X.A., Calit, J., Bargieri, D.Y., Donnelly, R.F., 2023. Primaquine and chloroquine nano-sized solid dispersion-loaded dissolving microarray patches for the improved treatment of malaria caused by Plasmodium vivax. J. Control. Release 361, 385–401. https://doi.org/10.1016/J.JCONREL.2023.08.009.

Anjani, Q.K., Nainggolan, A.D.C., Li, H., Miatmoko, A., Larrañeta, E., Donnelly, R.F., 2024. Parafilm® M and Strat-M® as skin simulants in in vitro permeation of dissolving microarray patches loaded with proteins. Int J Pharm 655, 124071. https://doi.org/10.1016/J.IJPHARM.2024.124071.

Atrooz, F., Alkadhi, K.A., Salim, S., 2021. Understanding stress: Insights from rodent models. Current Research in Neurobiology 2, 100013. https://doi.org/10.1016/J.CRNEUR.2021.100013.

Banerjee, S., Chattopadhyay, P., Ghosh, A., Datta, P., Veer, V., 2014. Aspect of adhesives in transdermal drug delivery systems. Int J Adhes Adhes 50, 70–84. https://doi.org/10.1016/j.ijadhadh.2014.01.001.

Bera, H., Kandukuri, S.G., Nayak, A.K., Boddupalli, S., 2015. Alginate-sterculia gum gel-coated oil-entrapped alginate beads for gastroretentive risperidone delivery. Carbohydr Polym 120, 74–84. https://doi.org/10.1016/j.carbpol.2014.12.009.

Bin Sabri, A.H., Anjani, Q.K., Gurnani, P., Domínguez-Robles, J., Moreno-Castellanos, N., Zhao, L., Hutton, A.R.J., Donnelly, R.F., 2023. Fabrication and characterisation of poly(sulfonated) and poly(sulfonic acid) dissolving microneedles for delivery of antibiotic and antifungal agents. Int J Pharm 644, 123292. https://doi.org/10.1016/J.IJPHARM.2023.123292.

D'Souza, S., Faraj, J., DeLuca, P., 2013. Microsphere delivery of risperidone as an alternative to combination therapy. European Journal of Pharmaceutics and Biopharmaceutics 85, 631–639. https://doi.org/10.1016/j.ejpb.2013.07.012.

Daniel, J.S.P., Veronez, I.P., Rodrigues, L.L., Trevisan, M.G., Garcia, J.S., 2013. Risperidone – Solid-state characterization and pharmaceutical compatibility using thermal and non-thermal techniques. Thermochim Acta 568, 148–155. https://doi.org/10.1016/j.tca.2013.06.032.

Demartis, S., Anjani, Q.K., Volpe-Zanutto, F., Paredes, A.J., Jahan, S.A., Vora, L.K., Donnelly, R.F., Gavini, E., 2022. Trilayer dissolving polymeric microneedle array loading Rose Bengal transfersomes as a novel adjuvant in early-stage cutaneous melanoma management. Int J Pharm 627, 122217. https://doi.org/10.1016/J.IJPHARM.2022.122217.

European Medicines Agency, ICH guideline M10 on bioanalytical method validation, (2019). https://www.ema.europa.eu/en/documents/scientific-guideline/ich-guideline-m10-bioanalytical-method-validation-step-5_en.pdf.

Fang, J., Bourin, M., Baker, G.B., 1999. Metabolism of risperidone to 9-hydroxyrisperidone by human cytochromes P450 2D6 and 3A4. Naunyn Schmiedebergs Arch Pharmacol 359, 147–151.

Fereig, S.A., El-Zaafarany, G.M., Arafa, M.G., Abdel-Mottaleb, M.M.A., 2021. Tacrolimus-loaded chitosan nanoparticles for enhanced skin deposition and management of plaque psoriasis. Carbohydr Polym 268, 118238. https://doi.org/10.1016/j.carbpol.2021.118238.

Gol, D., Thakkar, S., Misra, M., 2018. Nanocrystal-based drug delivery system of risperidone: lyophilization and characterization. Drug Dev Ind Pharm 44, 1458–1466. https://doi.org/10.1080/03639045.2018.1460377.

Gu, F., Ma, W., Meng, G., Wu, C., Wang, Y., 2016. Preparation and in vivo evaluation of a gel-based nasal delivery system for risperidone. Acta Pharm. 66, 555–562. https://doi.org/10.1515/acph-2016-0047.

Guillot, A.J., Cordeiro, A.S., Donnelly, R.F., Montesinos, M.C., Garrigues, T.M., Melero, A., 2020. Microneedle-Based Delivery: An Overview of Current Applications and Trends. Pharmaceutics 12, 1–28. https://doi.org/10.3390/PHARMACEUTICS12060569.

Hidayat Bin Sabri, A., Kurnia Anjani, Q., Donnelly, R.F., 2021. Synthesis and characterization of sorbitol laced hydrogel-forming microneedles for therapeutic drug monitoring. Int J Pharm 607, 121049. https://doi.org/10.1016/j.ijpharm.2021.121049.

Holder, C.F., Schaak, R.E., 2019. Tutorial on Powder X-ray Diffraction for Characterizing Nanoscale Materials, American Chemical Society. Nano 13, 7359–7365. https://doi.org/10.1021/acsnano.9b05157.

Jain, A.K., Swarnakar, N.K., Godugu, C., Singh, R.P., Jain, S., 2011. The effect of the oral administration of polymeric nanoparticles on the efficacy and toxicity of tamoxifen. Biomaterials 32, 503–515. https://doi.org/10.1016/j.biomaterials.2010.09.037.

Kayal, S., Ramanujan, R.V., 2010. Doxorubicin loaded PVA coated iron oxide nanoparticles for targeted drug delivery. Mater. Sci. Eng. C 30, 484–490.

Khames, A., 2017. Investigation of the effect of solubility increase at the main absorption site on bioavailability of BCS class II drug (risperidone) using liquisolid technique. Drug Deliv 24, 328–338. https://doi.org/10.1080/10717544.2016.1250140.

Koradia, K.D., Parikh, R.H., Koradia, H.D., 2018. Albendazole nanocrystals: Optimization, spectroscopic, thermal and anthelmintic studies. J Drug Deliv Sci Technol 43, 369–378.

Korbag, I., Mohamed Saleh, S., 2016. Studies on the formation of intermolecular interactions and structural characterization of polyvinyl alcohol/lignin film. Int. J. Environ. Stud. 73, 226–235. https://doi.org/10.1080/00207233.2016.1143700.

S.A. Kulkarni, A.S. Myerson, Methods for nano-crystals preparation, in: Engineering Crystallography: From Molecule to Crystal to Functional Form, 2017: pp. 275–287. DOI: 10.1007/978-94-024-1117-1_16.

Larraneta, E., Moore, J., Vicente-Perez, E.M., Gonzalez-Vazquez, P., Lutton, R., Woolfson, A.D., Donnelly, R.F., 2014. A proposed model membrane and test method for microneedle insertion studies. Int J Pharm 472, 65–73. https://doi.org/10.1016/j.ijpharm.2014.05.042.

Li, R.-Y., Liu, Z.-G., Liu, H.-Q., Chen, L., Liu, J.-F., Pan, Y.-H., 2015. Evaluation of biocompatibility and toxicity of biodegradable poly (DL-lactic acid) films. Am J Transl Res 7, 1357.

Lilleby Helberg, R.M., Dai, Z., Ansaloni, L., Deng, L., 2020. PVA/PVP blend polymer matrix for hosting carriers in facilitated transport membranes: Synergistic enhancement of CO2 separation performance. Green Energy Environ. 5, 59–68. https://doi.org/10.1016/j.gee.2019.10.001.

Lu, Y., Tang, X., Cui, Y., Zhang, Y., Qin, F., Lu, X., 2008. In vivo evaluation of risperidone-SAIB in situ system as a sustained release delivery system in rats. Eur. J. Pharm. Biopharm. 68, 422–429. https://doi.org/10.1016/j.ejpb.2007.05.016.

Mansur, H.S., Sadahira, C.M., Souza, A.N., Mansur, A.A.P., 2008. FTIR spectroscopy characterization of poly (vinyl alcohol) hydrogel with different hydrolysis degree and chemically crosslinked with glutaraldehyde. Mater. Sci. Eng. C 28, 539–548. https://doi.org/10.1016/j.msec.2007.10.088.

Mauludin, R., Muller, R.H., Keck, C.M., 2009. Development of an oral rutin nanocrystal formulation. Int J Pharm 370, 202–209. https://doi.org/10.1016/j.ijpharm.2008.11.029.

McGuckin, M.B., Wang, J., Ghanma, R., Qin, N., Palma, S.D., Donnelly, R.F., Paredes, A.J., 2022. Nanocrystals as a master key to deliver hydrophobic drugs via multiple administration routes. J. Control. Release 345, 334–353. https://doi.org/10.1016/j.jconrel.2022.03.012.

S.E. McNeil, J.R. Gibbons, M. Cogburn, Risperidone, StatPearls (2022). https://www.ncbi.nlm.nih.gov/books/NBK459313/.

Menon, I., Bagwe, P., Gomes, K.B., Bajaj, L., Gala, R., Uddin, M.N., D'Souza, M.J., Zughaier, S.M., 2021. Microneedles: A new generation vaccine delivery system. Micromachines (basel) 12. https://doi.org/10.3390/mi12040435.

Muller, R.H., Gohla, S., Keck, C.M., 2011. State of the art of nanocrystals-special features, production, nanotoxicology aspects and intracellular delivery. Eur. J. Pharm. Biopharm. 78, 1–9. https://doi.org/10.1016/j.ejpb.2011.01.007.

Nair, A.B., Jacob, S., 2016. A simple practice guide for dose conversion between animals and human. J Basic Clin Pharm 7, 27–31. https://doi.org/10.4103/0976-0105.177703.

Paredes, A.J., Mckenna, P.E., Ramöller, I.K., Naser, Y.A., Volpe-zanutto, F., Li, M., Abbate, M.T.A., Zhao, L., Zhang, C., Abu-ershaid, J.M., Dai, X., Donnelly, R.F., 2020. Microarray Patches : Poking a Hole in the Challenges Faced When Delivering Poorly Soluble Drugs. Adv Funct Mater 2005792, 1–27. https://doi.org/10.1002/adfm.202005792.

Patel, K.R., Cherian, J., Gohil, K., Atkinson, D., 2014. Schizophrenia: Overview and treatment options. Pharmacy and Therapeutics 39, 638.

Permana, A.D., Tekko, I.A., McCrudden, M.T.C., Anjani, Q.K., Ramadon, D., McCarthy, H.O., Donnelly, R.F., 2019. Solid lipid nanoparticle-based dissolving microneedles: A promising intradermal lymph targeting drug delivery system with potential for enhanced treatment of lymphatic filariasis. J. Control. Release 316, 34–52. https://doi.org/10.1016/j.jconrel.2019.10.004.

Permana, A.D., Paredes, A.J., Volpe-Zanutto, F., Anjani, Q.K., Utomo, E., Donnelly, R.F., 2020. Dissolving microneedle-mediated dermal delivery of itraconazole nanocrystals for improved treatment of cutaneous candidiasis. Eur. J. Pharm. Biopharm. 154, 50–61. https://doi.org/10.1016/j.ejpb.2020.06.025.

Prausnitz, M.R., Langer, R., 2008. Transdermal drug delivery. Nat Biotechnol 26, 1261–1268. https://doi.org/10.1038/nbt.1504.

Qian, L., Zhang, H., 2011. Controlled freezing and freeze drying: A versatile route for porous and micro-/nano-structured materials. J. Chem. Technol. Biotechnol. 86, 172–184. https://doi.org/10.1002/jctb.2495.

Quan, W., Kong, S., Ouyang, Q., Tao, J., Lu, S., Huang, Y., Li, S., Luo, H., 2021. Use of 18beta-glycyrrhetinic acid nanocrystals to enhance anti-inflammatory activity by improving topical delivery. Colloids Surf B Biointerfaces 205, 111791. https://doi.org/10.1016/j.colsurfb.2021.111791.

Quirós Cognuck, S., Reis, W.L., Silva, M., Debarba, L.K., Mecawi, A.S., de Paula, F.J.A., Rodrigues Franci, C., Elias, L.L.K., Antunes-Rodrigues, J., 2020. Sex differences in body composition, metabolism-related hormones, and energy homeostasis during aging in Wistar rats. Physiol Rep 8, e14597.

Ramadon, D., McCrudden, M.T.C., Courtenay, A.J., Donnelly, R.F., 2022. Enhancement strategies for transdermal drug delivery systems: Current trends and applications, Drug Deliv. Transl Res 12, 758–791. https://doi.org/10.1007/s13346-021-00909-6.

Reyna, D., Bejster, I., Chadderdon, A., Harteg, C., Kurnia Anjani, Q., Hidayat Bin Sabri, A., Brown, A.N., Drusano, G.L., Westover, J., Bart Tarbet, E., Vora, L.K., Donnelly, R.F., Lipka, E., 2023. A five-day treatment course of zanamivir for the flu with a single, self-administered, painless microneedle array patch: Revolutionizing delivery of poorly membrane-permeable therapeutics. Int J Pharm 641, 123081. https://doi.org/10.1016/J.IJPHARM.2023.123081.

Romero, G.B., Keck, C.M., Muller, R.H., 2016. Simple low-cost miniaturization approach for pharmaceutical nanocrystals production. Int J Pharm 501, 236–244. https://doi.org/10.1016/j.ijpharm.2015.11.047.

A. Ruggiero, C.H. Villa, E. Bander, D.A. Rey, M. Bergkvist, C.A. Batt, K. Manova-Todorova, W.M. Deen, D.A. Scheinberg, M.R. McDevitt, Paradoxical glomerular filtration of carbon nanotubes, The Proceedings of the National Academy of Sciences USA 107 (2010) 12369–12374. DOI: 10.1073/pnas.0913667107.

Schizophrenia, (n.d.). https://www.who.int/news-room/fact-sheets/detail/schizophrenia (accessed March 19, 2024).

Serretti, A., 2024. Focus on neurodevelopmental conditions and antipsychotics prescription patterns. Int Clin Psychopharmacol 39, 215–219. https://doi.org/10.1097/YIC.0000000000000555.

Simpson, J., Kelly, J.P., 2012. An investigation of whether there are sex differences in certain behavioural and neurochemical parameters in the rat. Behav. Brain Res. 229, 289–300. https://doi.org/10.1016/j.BBR.2011.12.036.

Text and Methodology Q2 (R1), 2005, 2023. In: https://www.ema.europa.eu/en/documents/scientific-guideline/ich-q-2-r1-validation-analytical-procedures-text-methodology-step-5_en.pdf.

Tuomela, A., Hirvonen, J., Peltonen, L., 2016. Stabilizing agents for drug nanocrystals: Effect on bioavailability. Pharmaceutics 8, 16. https://doi.org/10.3390/pharmaceutics8020016.

Utomo, E., Domínguez-Robles, J., Moreno-Castellanos, N., Stewart, S.A., Picco, C.J., Anjani, Q.K., Simón, J.A., Peñuelas, I., Donnelly, R.F., Larrañeta, E., 2022. Development of intranasal implantable devices for schizophrenia treatment. Int J Pharm 624, 122061. https://doi.org/10.1016/J.IJPHARM.2022.122061.

Van Eerdenbrugh, B., Vercruysse, S., Martens, J.A., Vermant, J., Froyen, L., Van Humbeeck, J., Van den Mooter, G., Augustijns, P., 2008. Microcrystalline cellulose, a useful alternative for sucrose as a matrix former during freeze-drying of drug nanosuspensions - a case study with itraconazole. Eur. J. Pharm. Biopharm. 70, 590–596. https://doi.org/10.1016/j.ejpb.2008.06.007.

Vora, L.K., Vavia, P.R., Larrañeta, E., Bell, S.E.J., Donnelly, R.F., 2018. Novel nanosuspension-based dissolving microneedle arrays for transdermal delivery of a hydrophobic drug. J Interdisc Nanomed 3, 89–101. https://doi.org/10.1002/JIN2.41.

Vora, L.K., Moffatt, K., Tekko, I.A., Paredes, A.J., Volpe-Zanutto, F., Mishra, D., Peng, K., Raj Singh Thakur, R., Donnelly, R.F., 2021. Microneedle array systems for long-acting drug delivery. Eur. J. Pharm. Biopharm. 159, 44–76. https://doi.org/10.1016/J.EJPB.2020.12.006.

Weng, W., Quan, P., Liu, C., Zhao, H., Fang, L., 2016. Design of a drug-in-adhesive transdermal patch for risperidone: Effect of drug-additive interactions on the crystallization inhibition and in vitro/in vivo correlation study. J Pharm Sci 105, 3153–3161. https://doi.org/10.1016/j.xphs.2016.07.003.

Wiechers, J.W., 1989. The barrier function of the skin in relation to percutaneous absorption of drugs. Pharm Weekbl Sci 11, 185–198. https://doi.org/10.1007/BF01959410.

Wu, Y., Vora, L.K., Donnelly, R.F., Singh, T.R.R., 2022. Rapidly dissolving bilayer microneedles enabling minimally invasive and efficient protein delivery to the posterior segment of the eye. Drug Deliv Transl Res 1–17. https://doi.org/10.1007/s13346-022-01190-x.

Zhang, L., Jiao, Z., Yao, Z., Zhong, Y., Zhong, M., Yu, Y., 2005. The Validation of an LC-MS method for the determination of risperidone and its Active metabolite 9-hydroxyrisperidone in human plasma. Chromatographia 61, 245–251. https://doi.org/10.1365/s10337-005-0506-y.

Zhang, L., Guo, R., Wang, S., Yang, X., Ling, G., Zhang, P., 2021. Fabrication, evaluation and applications of dissolving microneedles. Int J Pharm 604, 120749. https://doi.org/10.1016/j.ijpharm.2021.120749.

Zheng, L., Yang, L., Zhao, X., Long, N., Li, P., Wang, Y., 2019. Effect of risperidone on proliferation and apoptosis of MC3T3-E1 cells. Braz. J. Med. Biol. Res. 52.